UPPSALA
UNIVERSITET

Solvent–Solute Interaction

Studied by Synchrotron Radiation Based Photo and Auger Electron Spectroscopies

WANDARED POKAPANICH

ACTA
UNIVERSITATIS
UPSALIENSIS
UPPSALA
2011

Dissertation presented at Uppsala University to be publicly examined in Häggsalen, Ångström laboratoriet, Lägerhyddsvägen 1, Uppsala, Friday, February 4, 2011 at 13:15 for the degree of Doctor of Philosophy. The examination will be conducted in English.

Abstract
Pokapanich, W. 2011. Solvent–Solute Interaction. Studied by Synchrotron Radiation Based Photo and Auger Electron Spectroscopies. Acta Universitatis Upsaliensis. *Digital Comprehensive Summaries of Uppsala Dissertations from the Faculty of Science and Technology* 726. 73 pp. Uppsala. ISBN 978-91-554-7980-0.

Aqueous solutions were studied using photoelectron and Auger spectroscopy, based on synchrotron radiation and a liquid micro-jet setup.

By varying the photon energy in photoelectron spectra, we depth profiled an aqueous tetrabutylammonium iodide (TBAI) solution. Assuming uniform angular emission from the core levels, we found that the TBA^+ ions were oriented at the surface with the hydrophobic butyl arms sticking into the liquid.

We investigated the association between ions and their neighbors in aqueous solutions by studying the electronic decay after core ionization. The $(2p)^{-1}$ decay of solvated K^+ and Ca^{2+} ions was studied. The main features in the investigated decay spectra corresponded to two-hole final states localized on the ions. The spectra also showed additional features, related to delocalized two-hole final states with vacancies on a cation and a neighboring water molecule. These two processes compete, and by comparing relative intensities and using the known rate for the localized decay, we determined the time-scale for the delocalized process for the two ions. We compared to delocalized electronic decay processes in Na^+, Mg^{2+}, and Al^{3+}, and found that they were slower in K^+ and Ca^{2+}, due to different internal decay mechanisms of the ions, as well as external differences in the ion-solute distances and interactions.

In the O 1s Auger spectra of aqueous metal halide solutions, we observed features related to delocalized two-hole final states with vacancies on a water molecule and a neighboring solvated anion. The relative intensity of these feature indicated that the strength of the interaction between the halide ions and water correlated with ionic size.

The delocalized decay was also used to investigate contact ion pair formation in high concentrated potassium halide solutions, but no concrete evidence of contact ion pairs was observed.

Keywords: Interatomic Coulombic Decay, ICD, Auger electron spectroscopy, AES, X-ray photoelectron spectroscopy, XPS, Ultra-violet spectroscopy, UPS, localized, delocalized, double ionization potential, DIP, two hole, final states, Water, H2O, Potassium chloride, KCl, Calcium chloride, CaCl2, Ammonium, NH4, Core hole, clock, lifetime, solvated, ion, alkali, halide, Coster Kronig, MAX-lab, BESSY

Wandared Pokapanich, Department of Physics and Astronomy, Surface and Interface Science, Box 516, Uppsala University, SE-751 20 Uppsala, Sweden.

FAMILY = **(F)**ather **(A)**nd **(M)**other **(I)** **(L)**ove **(Y)**ou

To my family

List of Papers

This Thesis is based on the following papers, which are referred to in the text by their Roman numerals.

I **A photoelectron spectroscopic study of aqueous tetrabutylammonium iodide**
   H. Bergersen, R. R. T. Marinho, W. Pokapanich, A. Lindblad, O. Björneholm, L. J. Sæthre, and G. Öhrwall
   J. Phys.: Condens. Matter , **19**, 326101 (2007).

II **Charge delocalization dynamics of ammonia in different hydrogen bonding environments: free clusters and in liquid water solution**
   A. Lindblad, H. Bergersen, W. Pokapanich, M. Tchaplyguine, G. Öhrwall, and O. Björneholm
   Phys. Chem. Chem. Phys., **11**, 1758 (2009).

III **Auger electron spectroscopy as a probe of the solution of aqueous ions**
   W. Pokapanich, H. Bergersen, I. L. Bradeanu, R. R. T. Marinho, A. Lindblad, S. Legendre, A. Rosso, S. Svensson, O. Björneholm, M. Tchaplyguine, G. Öhrwall, N. V. Kryzhevoi, and L. S. Cederbaum
   J. Am. Chem. Soc., **131**(21), 7264 (2009).

IV **Charge dependence of solvent-mediated inter-molecular Coster-Kronig decay dynamics of aqueous ions**
   G. Öhrwall, N. Ottosson, W. Pokapanich, S. Legendre, S. Svensson, and O. Björneholm
   Accepted by J. Phys. Chem. B, 2010

V **Ionic charge dependence of ion-solvent ICD time-scale for aqueous ions probed by the core-hole clock**
   W. Pokapanich, N. V. Kryzhevoi, N. Ottosson, S. Svensson, L. S. Cederbaum, O. Björneholm, and G. Öhrwall
   In manuscript

VI Bond-breaking, electron-pushing and proton-pulling: Active and passive roles in the interaction between aqueous ions and water as manifested in the O 1s Auger decay
W. Pokapanich, N. Ottosson, S. Svensson, G. Öhrwall, B. Winter, and O. Björneholm
In manuscript

VII No signature of contact ion pairs in the K 2p Auger spectra of highly concentrated potassium halide solutions
W. Pokapanich, N. Ottosson, J. Söderström, S. Svensson, O. Björneholm, and G. Öhrwall
In manuscript

Reprints were made with permission from the publishers.

The following is a list of publications to which I have contributed to. They are not included in this Thesis.

1. **Self-assembled heterogeneous argon/neon core-shell clusters studied by photoelectron spectroscopy**
   M. Lundwall, W. Pokapanich, H. Bergersen, A. Lindblad, T. Rander, G. Öhrwall, M. Tchaplyguine, S. Barth, U. Hergenhahn, S. Svensson, and O. Björneholm
   J. Chem. Phys., **126** (21), 214706 (2007).

2. **Adsorption of polar molecules on krypton clusters**
   A. Rosso, W. Pokapanich, G. Öhrwall, S. Svensson, O. Björneholm, and M. Tchaplyguine
   J. Chem. Phys., **127** (8), 084313 (2007).

3. **Free nanoscale sodium clusters studied by core-level photoelectron spectroscopy**
   S. Peredkov, G. Öhrwall, J. Schulz, M. Lundwall, T. Rander, A. Lindblad, H. Bergersen, A. Rosso, W. Pokapanich, N. Mårtensson, S. Svensson, S. L. Sorensen, O. Björneholm, and M. Tchaplyguine
   Phys. Rev. B, **75**, 235407 (2007).

4. **Size determination of free metal clusters by core-level photoemission from different initial charge states**
   S. Peredkov, S. L. Sorensen, A. Rosso, G. Öhrwall, M. Lundwall, T. Rander, A. Lindblad, H. Bergeron, W. Pokapanich, S. Svensson. O. Björneholm, N. Mårtensson, and M. Tchaplyguine
   Phys. Rev. B, **76**, 081402 (2007).

5. **Observation of the non-supported metal nanoparticle electron density of states by X-ray photoelectron spectroscopy**
   M. Tchaplyguine, S. Peredkov, A. Rosso, J. Schulz, G. Öhrwall, M. Lundwall, T. Rander, A. Lindblad, H. Bergersen, W. Pokapanich, S. Svensson, S. L. Sorensen, N. Mårtensson, and O. Björneholm
   Eur. J. Phys D, **45**, 295 (2007).

6. **Solvent Effect of Alcohols at the L-Edge of Iron in Solution: X-ray Absorption and Multiplet Calculations**
   S. Bonhommeau, N. Ottosson, W. Pokapanich, S. Svensson, W. Eberhardt, O. Björneholm, and E. F. Aziz
   J. Phys. Chem. B, **112** (40), 12571 (2008).

7. **Electronic Rearrangement upon the Hydrolyzation of Aqueous Formaldehyde Studied by Core Electron Spectroscopies**
N. Ottosson, E. F. Aziz, H. Bergersen, W. Pokapanich, G. Öhrwall, S. Svensson, W. Eberhardt, and O. Björneholm
J. Phys. Chem. B, **112** (51), 16642 (2008).

8. **Large variations in the propensity of aqueous oxychlorine anions for the solution/vapor interface**
N. Ottosson, R. Vácha, E. F. Aziz, W. Pokapanich, W. Eberhardt, S. Svensson, G. Öhrwall, P. Jungwirth, O. Björneholm, and B. Winter
J. Chem. Phys., **131** (12), 124706 (2009).

9. **Local electronic structure of functional groups in glycine as anion, zwitterion, and cation in aqueous solution**
J. Gråsjö, E. Andersson, J. Forsberg, L. Duda, E. Henke, W. Pokapanich, O. Björneholm, J. Andersson, A. Pietzsch, F. Hennies, and J. E. Rubensson
J. Phys. Chem. B, **113** (49), 16002 (2009).

10. **The influence of concentration on the molecular surface structure of simple and mixed aqueous electrolytes**
N. Ottosson, J. Heyda, E. Wernersson, W. Pokapanich, S. Svensson, B. Winter, G. Öhrwall, P. Jungwirth, and O. Björneholm
Phys. Chem. Chem. Phys., **12**, 10693 (2010).

11. **On the origins of core-electron chemical shifts of small biomolecules in aqueous solution: Insights from photoemission and ab initio calculations of glycine$_{aq}$**
N. Ottosson, K. J. Børve, D. Spångberg, L. J. Sæthre, M. Faubel, H. Bergersen, W. Pokapanich, G. Öhrwall, O. Björneholm, and B. Winter
Submitted to J. Am. Chem. Soc., 2010

12. **X-ray photoelectron spectroscopy as a novel tool for the study of nanoparticles dispersed in aqueous media**
J. Söderström, N. Ottosson, W. Pokapanich, G. Öhrwall, and O. Björneholm
Submitted

Comments on my own participation

Team work is the most important key-word to get all the works presented in this Thesis done. The common denominator for all articles is that I was involved in performing the experiments and contributing to the discussion. In paper II, I participated only in the liquid part. In paper III, V, VI, and VII, my contribution also includes planning, sample preparation, doing the data analysis, as well as finalization of paper and the manuscripts. The calculations in all papers were not performed by me, but provided by my colleagues.

Contents

1. Populärvetenskaplig sammanfattning

1.1 Vätskor och lösningar

Vätskor är viktiga föreningar, nödvändiga för liv, och den huvudsakliga beståndsdelen på jordens yta. De finns både i sin rena form och som lösningsmedel i biologiska system, i många industriella processer och kemiska reaktioner. Därför är det värdefullt att undersöka egenskaperna hos beståndsdelarna i vätskor. Det huvudsakliga system som undersökts i denna avhandling är joners beteende i vattenlösningar med salt.

1.1.1 Vatten
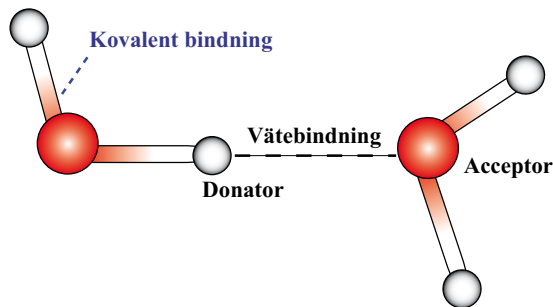
Figure 1.1: Vätebindning mellan två molekyler in en vattendimer.

Det viktigaste exemplet på en vätska är vatten. En vattenmolekyl består av en elektronegativ syreatom (O), vilken är kovalent bunden till två väteatomer (H). O-atomen tar upp en del av elektrondensiteten hos H-atomerna, vilket ger en polär molekyl. Kondenserat vatten hålls samman av så kallade vätebindningar, vilka mestadels är ett resultat av vattenmolekylernas polaritet. Exempelvis i en vattendimer, en grupp bestående av två vattenmolekyler, kallas den H-atom som är bunden till O-atomen i den andra molekylen för "vätebindningsdonator", medan O-atomen kallas "vätebindningsacceptor", som illustrerat i figur 1.1. Eftersom varje O-atom bär en partiell negativ laddning och H-atomerna bär partiell positiv laddning så sker en attraktiv växelverkan mellan H-atomen (donatorn) och O-atomen i den andra molekylen (acceptorn).

Styrkan av vätebindningen beror på donatorn och acceptorn så väl som deras omgivning [1, 2].

1.1.2 Vattenlösningar med salt

I vattenlösningar med salt är lösningsmedlet vatten, och den upplösta substansen är ett salt. Vanligen delar en neutral saltmolekyl upp sig i en katjon och en anjon, med positiv respektive negativ laddning, efter att ha lösts i vatten. De negativt laddade elektronerna attraheras av de positivt laddade elektronerna i atomkärnan, vilket leder till en minskning av jonens radie när den förlorat elektroner och en ökning när den tagit upp elektroner. Det joniska bindningsavståndet varierar med jonens omgivning, så som typ och antal hos grannatomer, vilket resulterar i en balans mellan elektrostatiska attraktiva och repulsiva termer. Figur 1.2(a) visar ett exempel, lösning av kaliumklorid (KCl) i vatten. Kaliumkloridsaltet dissocierar till K^+ och Cl^-, vilka har jonradierna 1.33 respektive 1.81 Å (10^{-10} m) [3]. Avstånden mellan $O-K^+$, $O-Cl^-$, och K^+-Cl^- är 2.65-2.81, 3.14-3.16, respektive 3.15 Å [4–7].
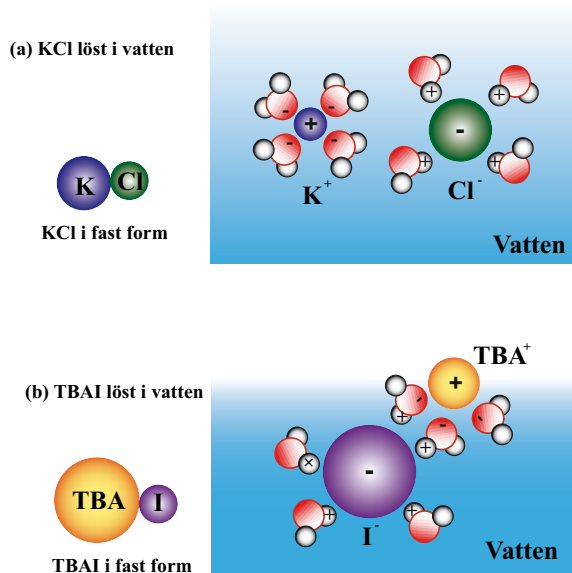
Figure 1.2: Jonbeteenden efter upplösning i vatten för (a) KCl och (b) TBAI.

Vissa salter, exempelvis tetrabutylammoniumjodid (TBAI), har en speciell egenskap, ytaktivitet, vilken innebär att när en TBAI-molekyl löses upp i vatten, så tenderar TBA^+-jonen att gå till ytan, som illustrerat i figur 1.2(b). I^--jonen är i sin tur attraherad av TBA^+-jonen, och bildar ett lager just under ytan. Eftersom de lösta jonerna kan bete sig på så mångahanda sätt är effekterna på lösningsmedel och den upplösta föreningen intressanta att studera.

14

1.2 Vätskor och elektronspektroskopi

Den flytande fasen karaktäriseras av partiell lokal ordning och oordning över stora avstånd. För att studera processer i vätskor är det därför värdefullt att använda metoder som sonderar den lokala omgivningen kring partiklarna vätskan består av. Detsamma är också sant för lösningsprocessen, för vilken en lokal sonderingsmetod är viktig för att ge inblick i de fysiska och kemiska processer som pågår. De djupt liggande elektroniska innernivåerna är lokaliserade nära den atomära kärnan, och detta gör att spektroskopiska metoder där dessa sonderas till utmärkta verktyg för att studera den lokala omgivningen i materia. En sådan metod är fotoelektronspektroskopi, där fotoner med hög energi träffar ett prov, och energin hos de elektroner som slås ut analyseras och ger information om provets elektroniska struktur. Eftersom det finns en skillnad i energi för innernivåer mellan olika typer av atomer är det möjligt att få lokal information med ämnesspecificitet. Figur 1.3 illustrerar energinivåerna hos grundämnena.
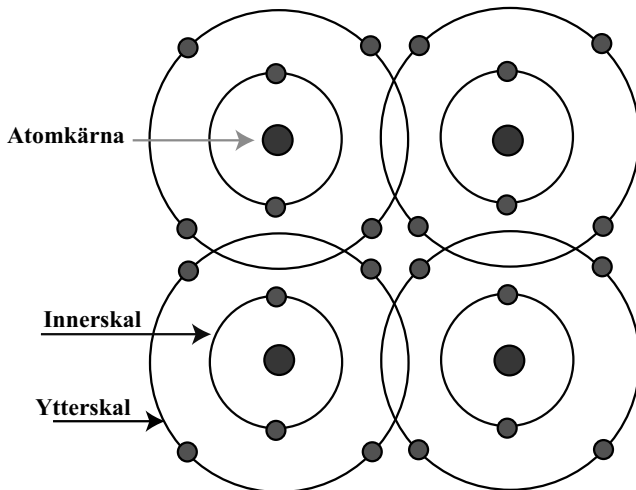
Figure 1.3: Energinivåer i kondenserade atomer. Ytterniverna hos grannatomer överlappar varandra, medan innernivåer är lokaliserade vid atomkärnan.

I exemplen visade i figur 1.2(a) och (b) så är det skillnader i elektronstruktur från konformationsförändringar, dissociation eller ytanrikning som det är möjligt att studera med fotoelektronspektroskopi. Genom att variera fotonenergin ändras energi hos de utslagna elektronerna, vilket påverkar hur långt de i genomsnitt kan gå genom materialet innan de sprids och förlorar energi. Tack vare denna effekt är det möjligt att djupprofilera vätskan, och därigenom besvara frågor om ytaktivitet. Inner- och ytternivåspektroskopiska tekniker är sålunda väl anpassade att studera vätskor.

2. Introduction

Liquids are important compounds, essential for life, and the major constituent of the surface of the earth. Both pure and as solvents they are present in biological systems, in many industrial processes and chemical reactions. There has been much recent interest to apply spectroscopy to investigate the structures of liquid systems, consisting of ions or neutral species solvated by neutral molecules e.g. water [8, 9]. Figure 2.1 illustrates some possible structure a molecule ABC may form after solvation. The structure of ABC may remain essentially unchanged (No.1), it may change its geometric conformation (No.2), it may dissociate, for instance into ionic fragments (No.3), or it may migrate to the surface with a hydrophobic end sticking out (No.4).
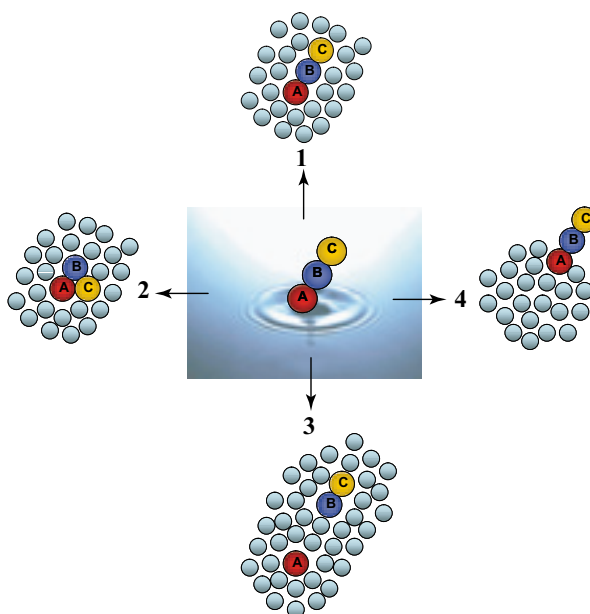
Figure 2.1: Schematic figure of a molecule ABC structure may form after solvation by solvent molecules.

The liquid phase is characterized by partial local order and long-range disorder, and to study processes in liquids, it is therefore valuable to use methods that probe the local surrounding of the constituent particles. The same is also true for solvation processes, for which a local probe is important to obtain insight into the physical and chemical processes going on. The deep lying

core levels are very localized, and this makes spectroscopies where these are probed excellent tools to study the local environment in matter. Due to the difference in energy for core levels between atomic species, it is also possible to do this with element specificity.

In the solvation example from figure 2.1, the differences in electronic structure from conformation changes, dissociation or surface aggregation are possible to obtain from photoelectron spectroscopy, and the effects both on solvent and solute are interesting to study. By varying the photon energy it is possible to depth profile the liquid, and thereby address questions related to surface activity. Core and valence spectroscopic techniques are thus well suited to study liquids. However, to apply photoelectron spectroscopy to liquids, many problems need to be solved, for instance vacuum requirements and charging effects. The characteristics of the jet are key parameters, which are examined in more detail in chapter 5.

This Thesis consists of two parts. The first part explains experimental details together with theoretical background. The second part contains seven papers for scientific discussion.

Part 1 consists of seven chapters below:

- Chapter 1: *Populärvetenskaplig sammmanfattning*, gives a popular summary of the general fundamentals of liquids and spectroscopy, and their connection to daily life.

- Chapter 2: *Introduction*

- Chapter 3: *Methods and concepts*, is a brief summary of the basic principle of photoelectron and Auger electron spectroscopy, and additional concepts related to the spectrum interpretation are provided.

- Chapter 4: *Experimental equipment*, explains synchrotron radiation, the beamline and the electron analyzer used for the experiment.

- Chapter 5: *The liquid jet setup for electron spectroscopy*, discusses the properties of the liquid jet important for the experiments. The present liquid setup is also described.

- Chapter 6: *Results and discussion*, gives a brief summary of the results obtained for aqueous solutions. The surface activity of solvated tetrabutylammonium (TBA^+) in tetrabutylammonium iodide (TBAI) is the subject of Paper I. For Papers II-VII, the objective is to discuss the electronic structure, the behavior of molecule/ions, and the surrounding environment in aqueous solutions.

- Chapter 7: *Summary and Outlook*

Part 2 contains the following papers:

- Paper I: A photoelectron spectroscopic study of aqueous tetrabutylammonium iodide, *J. Phys.: Condens. Matter, 19, 326101 (2007).*

- Paper II: Charge delocalization dynamics of ammonia in different hydrogen bonding environments: free clusters and in liquid water solution, *J. Am. Chem. Soc., 131(21), 7264 (2009).*

- Paper III: Auger electron spectroscopy as a probe of the solution of aqueous ions, *Phys. Chem. Chem. Phys., 11, 1758 (2009).*

- Paper IV: Charge dependence of solvent-mediated inter-molecular Coster-Kronig decay dynamics of aqueous ions, *accepted by J. Phys. Chem. B, (2010).*

- Paper V: Ionic charge dependence of ion-solvent ICD time-scale for aqueous ions probed by the core-hole clock, *in manuscript.*

- Paper VI: Bond-breaking, electron-pushing and proton-pulling: Active and passive roles in the interaction between aqueous ions and water as manifested in the O 1s Auger decay, *in manuscript.*

- Paper VII: No signature of contact ion pairs in the K 2p Auger spectra of highly concentrated potassium halide solutions, *in manuscript.*

3. Methods and concepts

In this chapter the essential concepts of the research presented in this Thesis are discussed, as well as the electron spectroscopy techniques for investigation of matter. In addition, the spectrum interpretation is also described.

3.1 Spectroscopy

The term spectroscopy was for a long time connected to the study of the energy distribution of photons. During the latter part of the previous century, the use of this term has been extended to cover also investigations of the energy distributions of particles like electrons or neutrons [10–12]. One of these techniques is electron spectroscopy, which has found many applications in the energy region that is comparable to the binding energies (BEs) of the electrons in atoms and molecules. There are two main processes in electron spectroscopy that yield electrons with kinetic energies (KEs) defined by the internal structure of the sample [9]. One is photoelectron emission; used in X-ray Photoelectron Spectroscopy (XPS) and Ultraviolet Photoelectron Spectroscopy (UPS), and the other is Auger decay; used in Auger Electron Spectroscopy (AES).
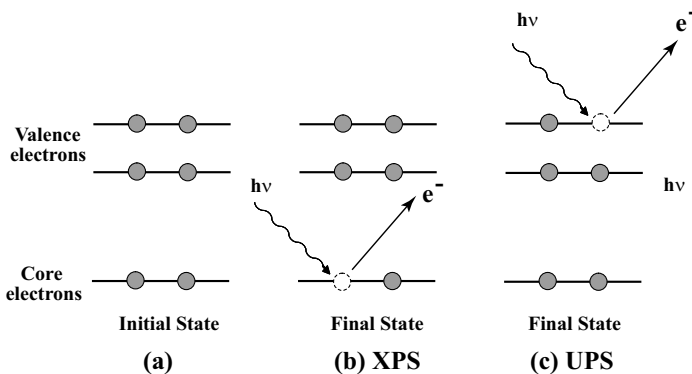

Figure 3.1: (a) Schematic figure of a ground state electron configuration in an atom (b) a core electron is removed from the inner shell (b) a valence electron is ejected from the outer shell.

3.1.1 Photoemission and photoelectron spectroscopy

In the photoemission process, an atom in the sample under study absorbs the energy of one photon and if it has more energy than the electron BE of the material, an electron is ejected. Increasing the intensity of the light beam meaning the number of photons, increases the number of electrons emitted. However, the energy of the emitted electrons does not depend on the intensity of the incoming light, but only on the energy of the individual photons. Photoemission or photoelectron spectroscopy (PES) is a powerful tool where this process is used to probe matter [13–15].

PES is a widely used method for determining the chemical composition of a sample. The XPS process arises when a photon interacts with a core level of the sample, leading to ionization of one of these inner electrons. By contrast, in the UPS process an outer electron is ejected from a valence shell. The photoemission process is schematically illustrated in figure 3.1.

The KE-dependent probability of inelastic scattering of an emitted electron in photoelectron spectroscopy limits the depth from which it can emerge, giving depth profiling information and surface sensitivity. The KE and the BE energy of an ejected electron are related by this equation:

$$KE = h\nu - BE \tag{3.1}$$

h is Planck constant and ν is frequency (Hz) of the radiation. XPS and UPS have been used extensively to characterize gases, solid materials, and recently these methods have become available for investigations of liquids [16, 17].
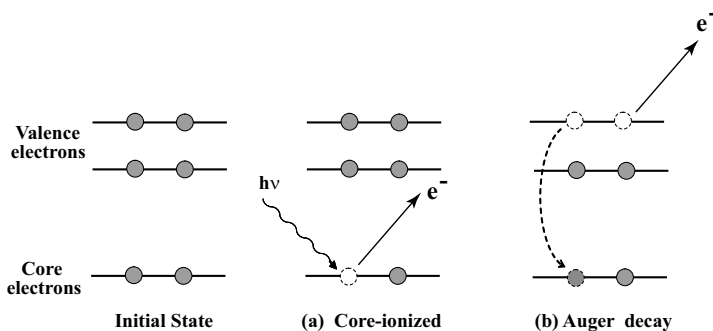
Figure 3.2: Schematic figure of the Auger decay process (a) a core-hole is created and (b) filled by a valence electron and another valence electron is removed.

3.1.2 Auger decay and Auger electron spectroscopy

Auger electron spectroscopy is another powerful technique for investigating gases, solids, and liquids. The Auger process can be considered as involving two basic steps. The first step is the removal of an inner shell atomic electron

to form a vacancy as illustrated in figure 3.2-(a). In the second step the inner shell vacancy is filled by an electron from a higher shell, and another electron escaping, as show in figure 3.2-(b). In the context of this Thesis, the case of an excited ion decaying into a doubly charged ion by ejection of an electron is common, and we will refer to it as the normal Auger decay, to distinguish it from delocalized decay processes.
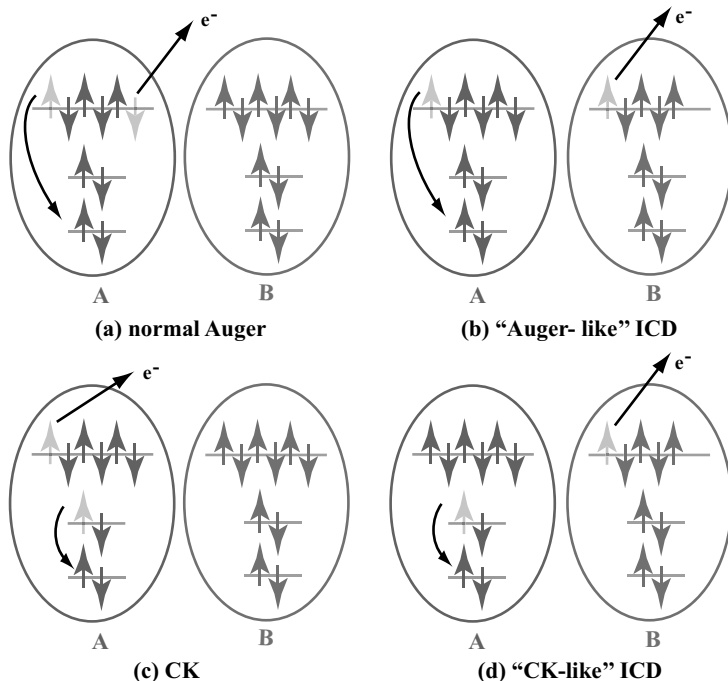
Figure 3.3: Schematic figure of the normal Auger, "Auger-like" ICD, CK, and "CK-like" ICD are illustrated in channel (a), (b), (c), and (d) respectively.

3.1.3 Interatomic or Intermolecular Coulombic Decay

Interatomic or Intermolecular Coulombic Decay (ICD) is a process where the relaxation of the vacancy involves weakly bonded neighboring atoms or molecules. It was originally discussed in the context of relaxation of inner-valence holes in weakly bonded systems, such as van der Waals bonded neon clusters [18]. Examples of such decays have also been seen in hydrogen bonded water clusters [19] and in solutions [Paper III]. The nature of the ICD process is similar to the normal Auger decay in figure 3.3(a), except the vacancies in the final states. Figure 3.3(b) illustrates what we refer to as an "Auger-like" ICD process. When a core electron is photoemitted from unit A, it is possible for the core hole to be filled by a valence electron from the same unit, while an electron from the neighboring unit B is emitted. ICD can take

place only if unit B is in close vicinity [20], and its decay rate, or the lifetime of the excited state, is discussed more in Paper V.

3.1.4 Coster-Kronig process

Coster Kronig (CK) decay is a related decay process, in which the vacancy is filled by an electron from the same main shell, but from a higher sub-shell, and a second electron is emitted. The core hole life time in the CK process is typically is shorter than in the case of normal Auger and ICD decay. Due to the larger overlap of the involved orbitals, the decay rate of CK is higher than for Auger. Since the core hole lifetime is inversely proportional to its total decay rate, CK, when energetically allowed, leads to a corresponding shortening of the core-hole life time.

As in the case of the Auger decay, the final state after the CK decay normally consists of two holes on the same unit. A final state with a hole on the unit where the core hole originally was (A) and one hole on a neighboring unit (B), is also possible, and we refer to this as intermolecular or CK-like ICD decay. In ionic solutions, the presence of the solvent molecules in the vicinity of the cations may open up intermolecular CK decay channels, which affects the lifetime of the core ionized state [Paper IV]. The normal Auger, "Auger-like" ICD, CK, and "CK-like" ICD are illustrated in figure 3.3(a), (b), (c), and (d) respectively. Paper IV and V will discuss the time-scale of core hole decay in these processes for solvated ion in aqueous solutions.

3.2 Spectrum interpretation

When analyzing spectra, insight into the factors that affect BEs when solvating e.g. an ion is needed. One of the main contributions in this respect is polarization screening, which is described below. When obtaining quantitative data from spectra, line shape modeling is necessary, and below some aspects of the line shapes are discussed, such as spin orbit splitting, inelastic scattering, inequivalent positions, vibrations, and other line broadenings.

3.2.1 Polarization screening

Most liquids are held together by weak intermolecular forces, which do not allow rapid interparticle charge re-arrangements upon ionization, as for instance is the case for metals. Instead, the charge distribution will be polarized by the hole, affecting the BE of photoelectrons.

This section describes general aspects of polarization screening. When a neutral atom in condensed matter is ionized, it receives a positive final charge. The ionized atom affects the electron density of the surrounding atoms, and the resulting polarization of the atoms screens the positive hole. The result-

ing charge-dipole attraction influences the BE by lowering of the final state energy, and as a result the KE of emitted electron is higher than for the corresponding free atom. The lowering of the BE due to the polarization screening depends on the number of nearest neighbors of the ionized atom.

3.2.2 Lineshape modelling

Many effects contribute to the shape of core level spectroscopy lines. Some can be minimized by increased experimental resolution, while others are inherent to the sample and set the lower limit to the line width. The shape of the line used to model these different contributions depends on the physical nature of the broadening [21]. Some of the significant contributions are discussed further below.

- **Spin orbit splitting**

Spin orbit splitting occurs when an electron with angular momentum greater than zero is ejected from a closed shell, leaving a remaining electron from the same orbital unpaired. The spin quantum number of the remaining electron can have spin up or spin down, and these two possibilities result in different total angular momenta of the ionized state, and hence difference final state energy. The spin-orbit coupling gives rise to peak splitting in photoelectron spectrum and its strength depends on the distance of the electron from the nucleus. For instance, when ionizing the electron in the 2p shell, the XPS spectrum exhibits two peaks, the $2p_{3/2}$ and $2p_{1/2}$ components.

- **Inelastic scattering**

When electrons are emitted and move to the electron analyzer, not all of them emerge unperturbed from the sample, but some emitted electrons may collide with atoms or molecules and lose energy, resulting signal loss due to inelastic scattering. In this phenomenon, the intensity loss during the transport of the electrons through the medium can be described by the exponential equation is $e^{-x/\lambda}$ where x is the traversed distance through the medium and λ is electron mean free path, which depends on the medium and the KE of the emitted electron. At high KE λ is relatively long, and increasing with KE.

The short electron mean free path is the basis for surface analysis in electron spectroscopies, e.g. XPS, and it can be used to obtain depth profiles of a sample. By recording XPS spectra using two different photon energies, the photoelectrons will have different KE, and hence different surface sensitivity. In this Thesis, this depth profiling approach has been applied to study the surface activity of aqueous TBAI. More details will be described in Chapter 6 - Paper I.

- **Inequivalent positions**

The core level BE gives information about the chemical environment of an atom, which perhaps is the most powerful feature of XPS. Atoms of the same type appearing in different chemical surrounding, the XPS spectrum will give rise to different BEs in the XPS spectrum [22]. In solutions, small variations in solvation geometry will therefore cause differences in BE, which are manifested as a broadening of lines of solvated species.

- **Vibrations**

In the XPS process, the molecular geometry may change drastically due to the increase of the charge of the ionic core, and lead to vibrational excitations. The theoretical analysis of the vibrational structure is based on the Franck-Condon principle. The vibrational excitation in a core-ionized process can be classified into intra- and inter-molecular components.

-The Franck-Condon principle

The Born-Oppenheimer approximation is often used in the description of molecules. It says that the electronic and vibrational wave functions describing the molecule may be separated, and this is based on the fact that the electrons are fast particles which can adapt to the field set up by the nuclei in a molecule, and that these move much slower than the electrons. The transition rate between two states can then be described by an electronic part and a vibrational part, where the vibrational part, giving the relative intensity of a certain vibration in the spectrum, is given by the overlap between the initial and final state vibrational wave functions. This is called the Franck-Condon principle, and the square of the overlap integral for the vibrational wave functions are called Franck-Condon factors.

-Intra and inter molecular vibrations

For the systems studied in this Thesis, the intra-molecular bonding is much stronger than the inter-molecular bonding. This allows treating intra-molecular and inter-molecular vibrations separately. The intra-molecular modes are taken to be similar to that of the free monomer, and the inter-molecular vibrations give a Gaussian contribution to the total width of the spectral features [23–25]. Though no clear vibrational structure has been observed in the electron spectra of solvated species, it is important to realize that these contributions exist, and can be accounted for in the analysis.

- **Line broadening**

The line broadening mechanisms discussed in this section i.e. lifetime broadening and experimental broadening, are inherent to all photoemission experiments, and are naturally considered in the analysis in this Thesis.

-Lifetime broadening

Lifetime broadening is most easily described using the Heisenberg uncertainty principle, occurring when the system has a finite lifetime. The core ionized atom returns to a lower energy level by release of a photon or ejection of an electron. The core-hole lifetime for the systems studied in this Thesis is in the order of a few femtoseconds, or less. The short core hole life time corresponds to a relatively large uncertainty in the energy of the core hole. The relationship between the core hole life time (τ) and the energy uncertainty (ΔE) is described by equation [26]:

$$\triangle E = \frac{\hbar}{\tau} \tag{3.2}$$

This ΔE is the inherent lifetime broadening of the state and gives the FWHM of the associated *Lorentzian lineshape*.

-Experimental broadening

In the photoelectron process, the finite precision in photon energy selection and electron KE determination result in experimental broadening, which contributes to the total spectral width. The spectrometer resolution can be controlled by changing the pass energy and the width of the entrance slit in the setup used in this Thesis. There is a trade-off between intensity and resolution, such that high resolution corresponds to decreased intensity. The experimental broadening gives rise to a *Gaussian lineshape* of the experimental signal. If feasible, this broadening is often set slightly lower than the lifetime broadening [25, 27].

4. Experimental equipment

The experiments in the Thesis have been performed at the Swedish and the German Synchrotron research centers MAX lab and BESSY. This chapter is into several subsections: General fundamentals of synchrotron radiation; MAX-lab and beamline I411, BESSY and beamline U41-PGM; and the basics of the hemispherical electron analyzer.

4.1 Synchrotron radiation

Synchrotron radiation is produced by charged particles moving around a circular ring with a velocity almost equal to the speed of light. Accelerating charged particles emit electromagnetic radiation. In a synchrotron storage ring, bending (dipole) magnets force the electrons to undergo centripetal acceleration, thereby emitting radiation. The high velocity of the electrons causes a relativistic contraction of the wavelength of the emitted radiation, which will have high intensity in the UV and X-ray ranges.

The storage rings which have been used for the present Thesis are of the 3rd generation, meaning they are optimized for magnetic insertion devices: wigglers and undulators [28]. The wiggler has few periods of stronger magnetic field, and the produced radiation is a spectrally broad beam of incoherent synchrotron light. In contrast to this an undulator consists of a large number of weak magnets, and the light emitted from each period overlaps and interferes with light emitted from the others, resulting in a narrow beam consisting of intense harmonics of partially coherent synchrotron light [29, 30]. Figure 4.1 shows an overview of a synchrotron radiation facility with storage ring, and experimental end station at the beamlines.

Synchrotron radiation is a powerful and flexible light source, since it has high brilliance and intensity and the photon energy is tunable over a wide range from IR to the hard x-ray region. Furthermore it produces highly polarized radiation which can be either linear, circular or elliptical. Consequently, synchrotron radiation is used in many research fields such as chemistry, physics, biology, and medicine.
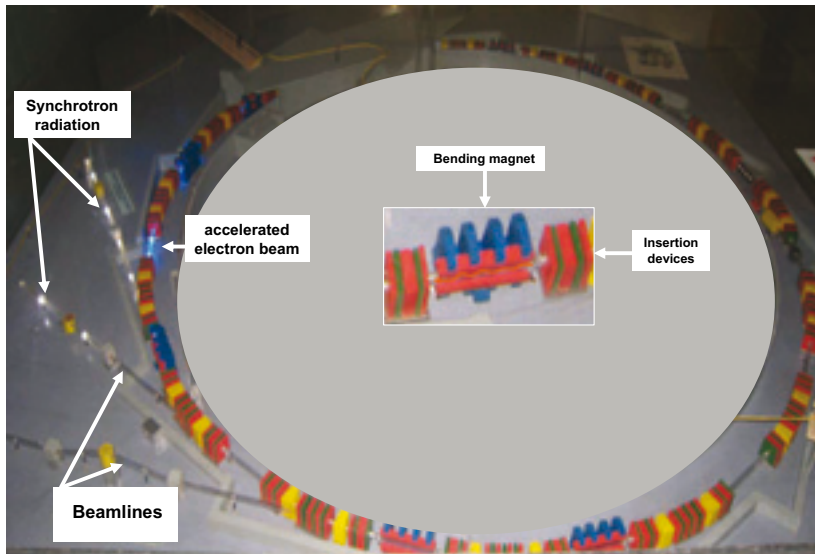
Figure 4.1: The figure shows a model of a storage ring, accelerated electrons beam, synchrotron light, and the beamlines. A storage ring consists of bending magnets and two types of insertion devices: wigglers and undulators.

4.2 MAX-lab and beamline I411

4.2.1 MAX-lab

MAX-lab is the national Swedish laboratory for synchrotron radiation studies in the fields of accelerator physics, synchrotron radiation, and nuclear physics. The facility consists of three electron storage rings: MAX I, MAX II, and MAX III. An overview of MAX-lab can be seen in figure 4.2.

The first storage ring at MAX-lab was the 2rd generation light source MAX I, which was built in 1986 and operates at the energy 550 MeV. Ten years later, MAX II was taken into operation. It is a 3rd generation synchrotron equipped with several undulator and wiggler beamlines, with the maximum electron energy 1.5 GeV. Beamline I411 which was used in this Thesis is located at MAX II, and it will described further below. MAX III is also a 3rd generation synchrotron source, commissioned in 2007 with an electron energy of 700 MeV [31].

4.2.2 Beamline I411

Most of the experiments in this Thesis were performed at beamline I411, MAX-lab. Beamline I411 is a soft x-ray beamline, which has been operational since 1999. It was designed for many research fields such as gas phase atoms, molecules, metal vapours, liquids and thin films [32, 33]. The light source for beamline I411 is an undulator of 87 magnets arranged in 43 periods of 59
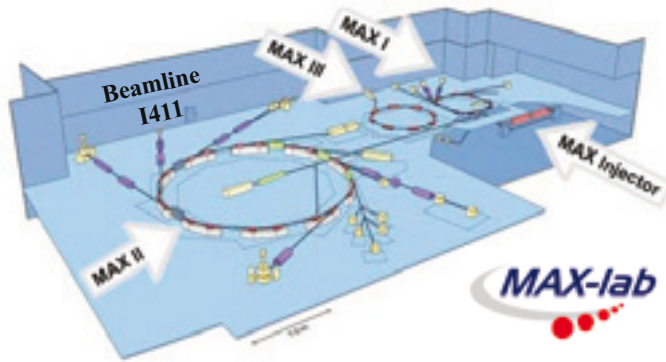
Figure 4.2: A schematic overview of the MAX laboratory, consisting of (from right to left hand side) MAX I, MAX III, and MAX II. The figure is taken and modified from MAX-lab website [31].

mm period length, providing a nominal photon energy range of 50 - 1500 eV [31]. Figure 4.3 shows an overview of beamline I411, including the optical elements and the electron spectrometer. The details concerning the spectrometer will be described further below.
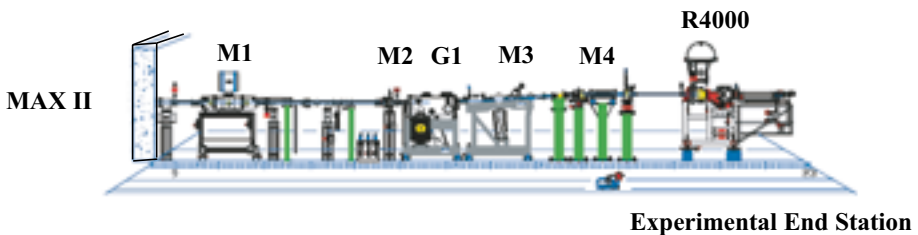

Figure 4.3: Layout of the beamline I411. The figure is taken and modified from MAX-lab website [31].

The synchrotron radiation travels from the undulator along the beamline I411, and reaches the end station where the experiments take place. Firstly the synchrotron beam is focused in the horizontal plane by a first spherical-mirror M1, and then passes the monochromator (of SX700 type) which consists of two optical components: a plane mirror M2 and a plane diffraction grating G1. A plane elliptical mirror M3 then focusses the radiation in the vertical direction through the exit slit. As mentioned, one of the main advantages of synchrotron radiation is that the photon energy is tunable, which is achieved by rotating the plane grating and the plane mirror M2 together. After passing the monochromator exit slit, the synchrotron beam is refocused in both vertical and horizontal planes by a toroidal mirror M4 and reaches the target at the end station. The spectrometer chamber at the end station can rotate from 0° to 90° relative to the horizontal polarization plane of the synchrotron light. Consequently, it is possible to adjust the electron analyzer relative to the po-

larization plane of the radiation to 54.7°, called *"the magic angle"*, to avoid angular anisotropy effects [27, 34]. The consequences of measuring outside the magic angle in the context of liquid samples will be discussed further in chapter 6.

The vertical size of the photon beam depends on the slit size [32], but is typically several 100 micrometers, i.e. considerably larger than the liquid jet. This means that the signal will contain a large contribution from the vapor surrounding the the liquid, which is a complication when interpreting spectra. However, the main topic of this Thesis is the study of solvated ions, and since these do not evaporate from the solutions, all signal from the ions comes from solvated species.

In addition, different kinds of vacuum pumps are installed along the beamline to protect the high vacuum in a storage ring ($< 10^{-10}$ mbar) from the high pressure caused by the experiment ($\approx 10^{-5}$ mbar for liquids).

4.3 BESSY and beamline U41-PGM

4.3.1 BESSY

The Berliner Elektronenspeicherring-Gesellschaft für Synchrotronstrahlung m. b. H. (English: Berlin Electron Storage Ring Society for Synchrotron Radiation), foreshortened BESSY, is a German research center located in Berlin and established on 5 March 1979. Earlier, BESSY was a part of the Gottfried Wilhelm Leibniz Scientific Community, but since 1 January 2009 it has been a section of the Helmholtz-Zentrum Berlin (HZB) [35].

BESSY is a 3rd generation synchrotron radiation facility, providing support for science and industry. BESSY consists of two main units; BER II and BESSY II. BER II operates for neutron experiments, whereas the electron storage ring BESSY II consists of 46 beam lines dedicates to ultra bright photon beam ranging from Terahertz radiation, intermediate between microwaves and IR, to hard X-rays (1.7 GeV) [36].

4.3.2 Beamline U41-PGM

Beamline U41 consists of three operating stations; U41-TXM, U41-STXM, and U41-PGM. The experiments in paper VI in this Thesis have been performed at U41-PGM which has a horizontal polarization and provides the energy range 170-1800 eV.

Figure 4.4 illustrates the optical devices along the beam- line. The premonochromator optic M1 is a gold coated toroidal mirror, which vertically collimates and horizontally focuses the radiation onto exit slit. G1 and M2 are gold coated plane grating and plane mirror for wavelength dispersion. M3 is a gold coated cylindrical mirror for vertical focussing onto exit slit. The post-
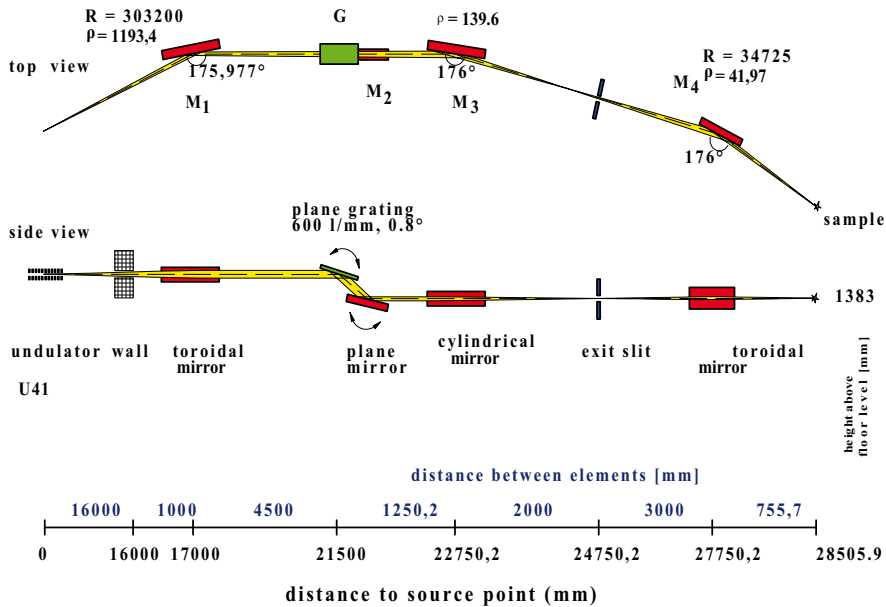
Figure 4.4: The optical layout of beamline U41-PGM

monochromator optic is a gold coated toroidal mirror, which vertically and horizontally focuses onto the sample [36–39].

Unlike the situation at I411 at MAX-lab, the vertical spot size at beamline U41-PGM is closely matched to the diameter of the liquid jet [36], meaning that the gas-phase signal typically is very small in the spectra recorded here. If, as sometimes is the case, one wishes to record spectra with a clear gas phase signal, the jet will typically have to be partly lowered out of the photon beam. Moreover, as mentioned above, the spectrometer chamber at the end station of beamline I411 is adjustable from $0°$ to $90°$ relative to the horizontal polarization plane of the synchrotron light. However, this is not possible at beamline U41-PGM due to practical limitations, and measurements with $90°$ between the polarization and detection directions is the only alternative.

4.4 The electron energy analyzer

The end station of beamline I411 is equipped with a Scienta R-4000 hemispherical electron analyzer, whereas a hemispherical electron energy analyzer Specs/Leybold EA10/100 with water compatible stainless steel electrodes and a secondary electron multiplier (SEM) was mounted at the end station of beamline U41-PGM. A schematic sketch of a hemispherical electron energy analyzer can be found in figure 4.5. The starting point is that electrons are

emitted from the sample and travel through the analyzer chamber with different velocities. An electron lens is used to collect the electrons and accelerate or retard them to a fixed KE, called the pass energy, before transporting the electrons to the analyzer. The two hemispherical electrodes provide the electric field to deflect and focus these electrons which respect to their KE.
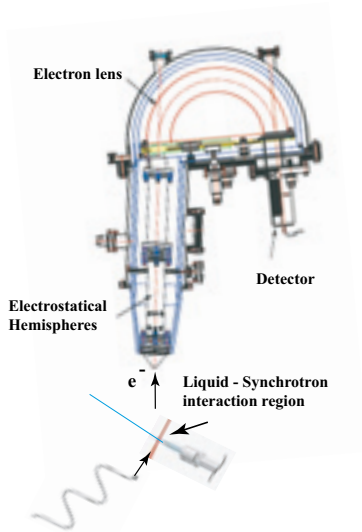

Figure 4.5: A schematic view of a Scienta hemispherical electron energy analyzer. The figure is used with the kindly permission of A. Lindblad [40].

The resolution of the spectrometer, measured as the FWHM of the Gaussian energy distribution, is primarily dependent on the spectrometer entrance slit size (s), the pass energy (E_p), and the radius (r) of the spectrometer hemispheres [25]:

$$FWHM = E_p \cdot \frac{s}{2r} \tag{4.1}$$

The pass energy limits the resolution of the spectrometer for a selected slit width. As mentioned above, there is a tradeoff between resolution and signal intensity, meaning the choice of pass energy must be a compromise between desired resolution and acceptable measurement time. In the experiments described in this Thesis, the inherent width of the photoelectron lines are typically much larger (≈ 1 eV) than the resolution of the spectrometer, meaning large pass energies have been used throughout. The total resolution in the spectrum will also be influenced by the monochromator bandwidth. Typically, the photon band width has been matched to the electron spectrometer resolution.

5. The liquid jet setup for electron spectroscopy

In order to apply electron spectroscopy to liquid samples, some special arrangements in the experiment setup have to be done to overcome the problems caused by the liquid sample. Liquids generally have a high vapour pressure and the experimental apparatus demands high vacuum, which puts great demands on the pumping capacity. However, the major problem is the vapour which causes a high probability of inelastic scattering of electrons leaving the liquid surface. The liquid micro jet technique was introduce to overcome these problems. Further details concerning the characteristics of the liquid jet and an overview of the liquid setup will be given below.

5.1 Liquid micro jet in vacuum

The basic problems of electron spectroscopy studies of liquids are the short mean free path of electrons traveling through a medium without suffering inelastic collisions, and the high vapor pressure of most liquids. The mean free path for electrons in a gas depends on the KE and the pressure. For example, a mean free path of 1 meter for electrons of 1 keV KE requires a pressure of less than 1×10^{-3} torr. Unfortunately most ordinary liquids have vapour pressure larger than 0.1 torr. The perhaps most important liquid, water, has a vapor pressure of 18 torr at a room temperature [34, 41].

One way to alleviate the problem is to introduce cooling of the liquid sample, for instance by water cooling. The water cooling system reduces the vapor pressure of the sample before the measurement. This is done both in the setup used at MAX-lab and the one used at BESSY. Efficient pumping, using liquid nitrogen cold traps to freeze out the liquid sample after the measurement, is vital. To reduce the distance the electrons have to travel in the vapor above the liquid surface, differential pumping with a small opening for the electrons to pass through close to the liquid surface is used. By cooling the liquid and utilizing differential pumping, a number of liquids have become accessible to electron spectroscopy.

5.2 The shape of the jet

As mentioned, there is also the question how to expose the liquid sample to the ionizing radiation i.e. synchrotron radiation and at the same time allow the electron to leave the sample chamber. The important improvement is the reduced evaporative area of the liquid [17]. In our present set-up, this is achieved by using a liquid micro-jet, see figure 5.1, with a diameter of approximately 15 microns.

Figure 5.1: The liquid micro-jet with a diameter of approximately 15 micron.

When liquid is ejected from the nozzle, a cylindrical micro-jet is formed. The surface tension breaks up the jet into droplets at the distance (l_{jet}). The liquid jet length l_{jet} was studied by Lord Rayleigh [42, 43]:

$$l_{jet} = 3v\sqrt{\frac{d^3\rho}{\sigma}} \tag{5.1}$$

where v is the velocity and ρ is the density of the liquid jet, d is the diameter of the needle, and σ is the surface tension.

The velocity of the jet can be estimated by the Bernoulli equation [44]:

$$v = \sqrt{\frac{2p}{\rho}} \tag{5.2}$$

where p is the backing pressure. To improve equation 5.1 and 5.2, Weber included the jet viscosity η into the linear stability analysis [45].

$$l_{jet} = 12\sqrt{\frac{2p}{\rho}}(\sqrt{\frac{d^3\rho}{\sigma}} + 3\eta\frac{d}{\sigma}) \tag{5.3}$$

Consider the case of water. For a backing pressure of 50 bar, the flow velocity becomes around 70 m/s, with l_{jet} being 5 mm. The current setup (2010), with the control in the pump set for flow, the velocity calculation becomes much easier.

It is necessary to position the ionization point in the the liquid before it breaks up into droplets, because the the isolated droplets would rapidly become charged from the radiation, making measurements impossible. From these relations, we can evaluate where to position the nozzle relative to the ionization point along the jet flow direction. In this Thesis, all projects used a distance from the nozzle to the ionization point of around 2-3 mm, i.e $< l_{jet}$. The positions in the other directions were optimized for liquid signal strength.

5.3   Charging of the jet

Since photoelectron spectroscopy observes the KE of outgoing electrons, it is highly sensitive to sample charging, which can significantly reduce the interpretability of the spectra. One charging problem for the liquid jet is due to an additional surface potential in the streaming liquid. A typical streaming current (I_{str}) for pure liquid water is in the order of -10 nA. For non-conducting liquids, the corresponding streaming potential can be calculated by [41]:

$$\Phi_{str} = -\frac{1}{2\pi\varepsilon_0}\frac{I_{str}}{\upsilon_{jet}}ln\frac{d_{jet}}{2} \qquad (5.4)$$

where υ is the velocity of the jet and d_{jet} is jet diameter. The streaming potential accelerates the electrons emitted from the surface.

A more serious charging problem occurs due to the spectroscopic technique itself. Many liquids, e.g. water, are non-conducting, and ionization then leads to build up of charge. To avoid this charging effect, we add some ions, e.g. NaCl, to the liquid to make it conducting. This addition of ions could affect the solution in various ways. However, all solutions studied in this Thesis are electrolytes, so no additional ions were added to the samples. As mentioned above, a third charging problem occurs if the ionization point is downstream of the point where the jet breaks up in small droplets, i.e. at a distance from the nozzle $> l_{jet}$. These droplets are isolated, and become charged by multiple ionization. To avoid this charging effect, we measure before the jet break up into droplets. These procedures ensure that we have a conducting grounded sample, and avoid charging.

5.4 Inelastic scattering

As mentioned earlier, inelastic scattering of electrons may cause signal loss due to the loss of energy energy after colliding with atoms or molecules before reaching the electron analyzer. For the liquid jet, the vapour causes a high probability of inelastic scattering of electrons leaving the liquid surface which has to be taken in to account.

A fast flowing and very thin liquid jet filament is injected into the vacuum system. The pressure due to evaporation decreases radially from the jet surface. For a cylindrical jet the effective vapor layer thickness (Pd) can be calculates as follow [41, 46]:

$$Pd = \int_{R_{jet}}^{R_{spec}} P(r)dr = P_0 R_{jet}(lnR_{spect} - lnR_{jet}) \qquad (5.5)$$

where R_{jet} is the radius of the jet, P_0 is the corresponding local equilibrium vapor pressure at the jet surface, and R_{spect} is the distance from the center of the jet to the exit hole of the differential pumping stage. For electron spectroscopy, Pd should be less than 0.1 torr.mm to achieve reasonable transmission.

For a pure water jet of 1 mm diameter and a transfer length of only 0.5 mm this would require a limiting surface vapor pressure of $P_0 \leq 0.3$ torr which is much less than the vapor pressure of 4.6 torr at 273 K [41]. To solve this problem and make both the evaporation and the scattering manageable, a micro-jet of very small diameter can be used. Shrinking the diameter to 20 micron and keeping the transfer length of 0.5 mm would for example increase the limiting surface vapor pressure by more than three orders of magnitude. Such a short transfer length is however not practical, and the typical distance between the jet and the exit hole of the differential stage was 2 mm in the experiments.

5.5 Sample preparation and handling

The experiments in this Thesis were performed at MAX-lab and BESSY, and the sample handling at the two setups was quite similar. The solutions were generally prepared from highly deionized water and commercially obtained chemicals. At MAX-lab, the water was initially commercially obtained, as in the early experiments when deionized water for car batteries was used, but more recently we have used water purified and deionized using a purification system from Millipore Corporation, so called Milli-Q water. In the experiments presented in this Thesis, extremely high purity of the samples has not been necessary, but usually the purity has been $\geq$99%. The salts were unhydrated from the supplier, and we have assumed that the degree of hydration from handling the chemicals in air is negligible. The amounts were measured with a high precision scale. After solving the salts with water, the samples

have been filtered, usually with a syringe filter (pore size 0.2 micron), to decrease the amount of small particles in the solutions, which may block the nozzle which has a diameter between 10-20 micron. The bottles with the solutions were also submerged in an ultra-sonic bath, to release bubbles formed from solvated air. The bubbles may cause interruptions in the flow of the liquid through the nozzle, during which there is a risk that liquid in the nozzle freezes. The sample is kept in glass bottles at atmospheric pressure, and a High Pressure Liquid Chromatography (HPLC) pump is used to pump it through the nozzle. In the tube between the liquid pump and the nozzle, a sintered microporous filter (pore size 1 micron) is placed, to prevent any remaining particles from the solution to reach the nozzle. At MAX-lab, the pump and high pressure tubing are of stainless steel, and the low-pressure tubing from bottles to pump are of teflon, which we believe are sufficiently inert for experiments such as those presented in this Thesis. At BESSY, both high and low pressure tubing as well as the holder for the filter between the liquid pump and the nozzle are of teflon.

5.6 Liquid jet setup at beamline I411, MAX lab

Several approaches to study liquids were used in the laboratory of Siegbahn: a liquid beam [47], a moving wetted wire [48], and a rotating metal cone immersed in a liquid basin [49]. Unfortunately, these methods only allowed studies of liquids with low vapour pressure, especially not water. Faubel and co-workers have made pioneering contributions by developing a vacuum-compatible setup to study liquids by using a micro jet as a sample [17, 41, 46]. Faubel *et. al.* showed that using high pressure, water can be formed into a straight, laminarily flowing, cylindrical filament with a smooth surface. To meet the effective vapour thickness condition, the jet diameter must be smaller than the mean free path of the water molecules in the gas phase at thermal equilibrium. With synchrotron excitation, this technique was applied together with electron spectroscopy to study the valence band of aqueous alkali-metal-iodide solutions [50], aqueous alkali-halide ions [51], and the surface activity in aqueous tetrabutylammonium iodide [Paper I].

Our research group has developed a setup for liquid studies by synchrotron radiation based electron spectroscopy. We were inspired to apply the liquid jet technique by Faubel and co-workers and the present setup is similar to the one they have adapted to synchrotron radiation as mentioned above. A schematic overview of liquid setup is shown in figure 5.2, and the actual setup is shown in figure 5.3. The separate parts will be described further below.

1. Liquid source chamber with gate valve, pumps and manipulator
2. Liquid micro-jet nozzle
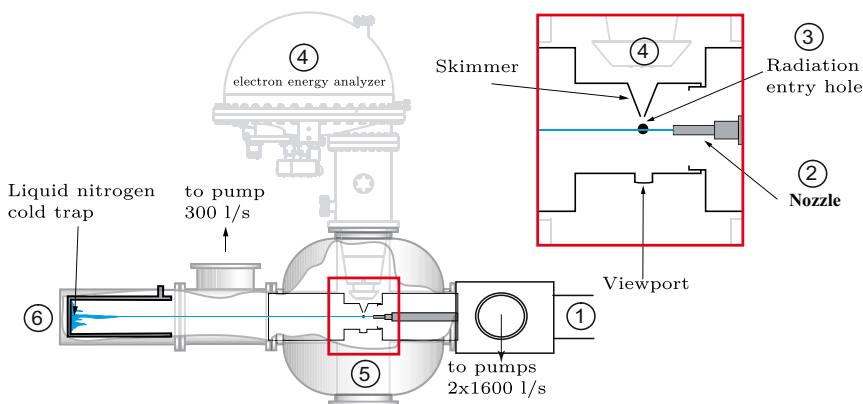3. Synchrotron Radiation

Figure 5.2: The experimental setup at beamline I411. The enlargement shows the central part, where the ionization takes place. The figure is adapted from paper I.

4. Photoelectron spectrometer and the skimmer
5. Differential pumping stage
6. Liquid nitrogen cold trap

The liquid source was mounted on a manipulator, passing through a vacuum chamber with powerful turbo pumps (No.1). The jet was in the earliest experiments, represented by paper I in this Thesis, produced by pressurizing a vessel containing the liquid with 50 bar of nitrogen. The vessel was connected to a needle of 10 microns diameter. Nowadays components from Microliquid GmbH [52], i.e. a liquid pump (number 200.021) and glass nozzles of 10, 15, and 20 microns inner diameter are used (No.2).

After the liquid jet is formed ejected from the nozzle, it is intersected by synchrotron radiation before distance it breaks up into droplets (No.3). The emitted electrons move through the skimmer with a 0.5 mm opening diameter (No.4), and are detected by the photoelectron spectrometer. The propagation of the jet is perpendicular to the direction of the photon beam and the spectrometer. The distance l_{jet} depends on several parameters, e.g. diameter of the nozzle and the flow rate for instance, as described in Eq. 5.3. For the present setup, the glass nozzle diameter is typically 15 microns, the flow rate is 0.6 ml/min. and the distance between the jet and the skimmer is 2 mm.

To separate the high pressure from the liquid from the rest of the sample chamber a differential pumping stage is mounted inside. Inside the chamber a mu-metal shield protects the ionization region and the spectrometer from external magnetic fields. The differential pumping stage is pumped by two 1600 l/s turbomolecular pumps upstream of the ionization point, and a 300 l/s turbomolecular pump downstream of the ionization point. During operation, the pressure inside of the ionization pumping stage is in the 10^{-5} mbar range (No.5). The best way to take care of the used liquid is to use a liquid nitro-

(a)   Electron Spectrometer   **(b)**
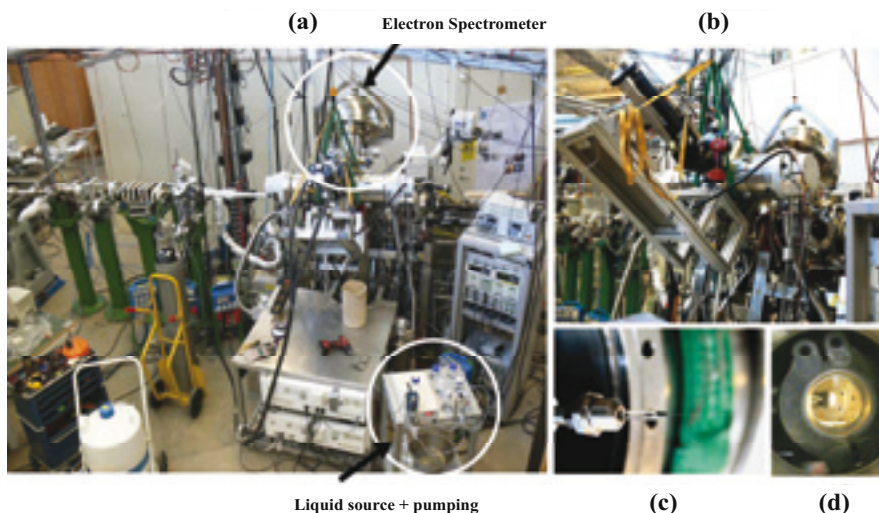
Liquid source + pumping   **(c)**   **(d)**

Figure 5.3: An overview of liquid setup at beamline I411. The mushroom shaped object at the top is the electron spectrometer, and the circle on the right bottom corner indicates the liquid pump. (b) Liquid source chamber with gate valve, pumps and manipulator. (c) Nozzle and liquid micro-jet in air. (d) The bottom view of the liquid jet nozzle in measuring position, perpendicular to the skimmer.

gen cold trap (No. 6). In the cold trap, the liquid jet will freeze, as shown in figure 5.4, and not degrade the vacuum. In addition all turbomolecular pumps are equipped with liquid nitrogen cold traps between the turbo pumps and the fore vacuum pumps.
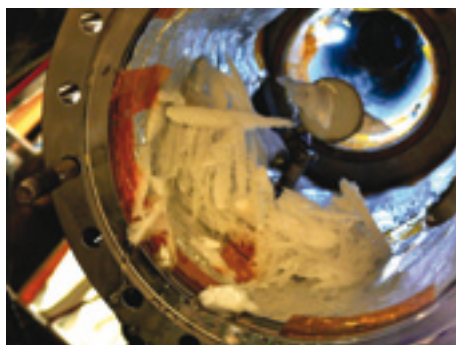

Figure 5.4: An ice from the liquid sample, captured in the liquid nitrogen cold trap.

5.7 Liquid jet setup at beamline U41-PGM, BESSY

The liquid jet setup that was used at BESSY is similar to that used at MAX-lab. It belongs to our colleagues Bernd Winter and Manfred Faubel, the pioneers of the micro-liquid jet technique for electron spectroscopy. The schematic figure 5.5 shows the liquid micro-jet setup, which consists of four main parts; the cubic i nteraction chamber (I), the cryo-pumped chamber (II), differential pumping stage (III), and the spectrometer chamber (IV).
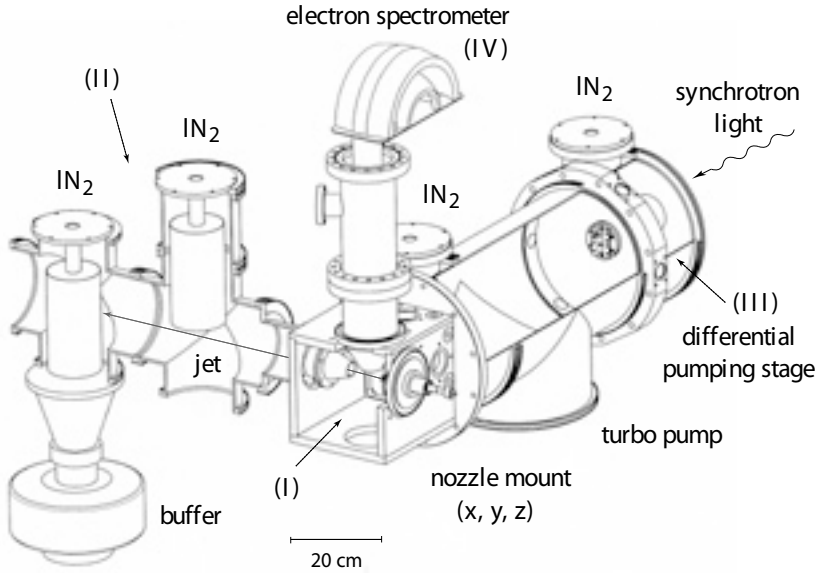

Figure 5.5: Schematic of the water jet apparatus at BESSY II. (I) main interaction chamber, (II) cryo-pumped chamber, (III) differential pumping stage, (IV) spectrometer chamber.

The liquid micro-jet nozzle is mounted in the main chamber (I), and the jet is directed to the liquid nitrogen cold trap (II). The liquid jet intersects the perpendicular synchrotron beam that exits from the last refocusing chamber at the beamline U41-PGM (III), and the ejected electrons enter the hemispherical electron analyzer (Specs Leybold EA10) (IV), which is mounted perpendicular to the liquid jet and the photon beam [39, 53]. The spectrometer lens axis is at 90° with respect to the polarization vector of the plane polarized radiation.

6. Results and discussion

6.1 Surface activity: Paper I

Tetrabutylammonium iodide (TBAI) is a salt consisting of an iodide anion I^- and a tetrabutylammonium cation $C_{16}H_{36}N^+$, as illustrated in figure 6.1. It is surface active which means that when the TBAI molecules dissolve in water, they incline to the surface, as addressed by Tamaki [54] and Holmberg [55].
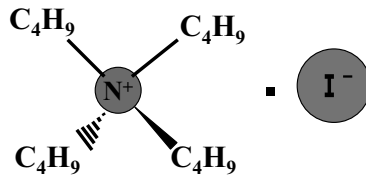
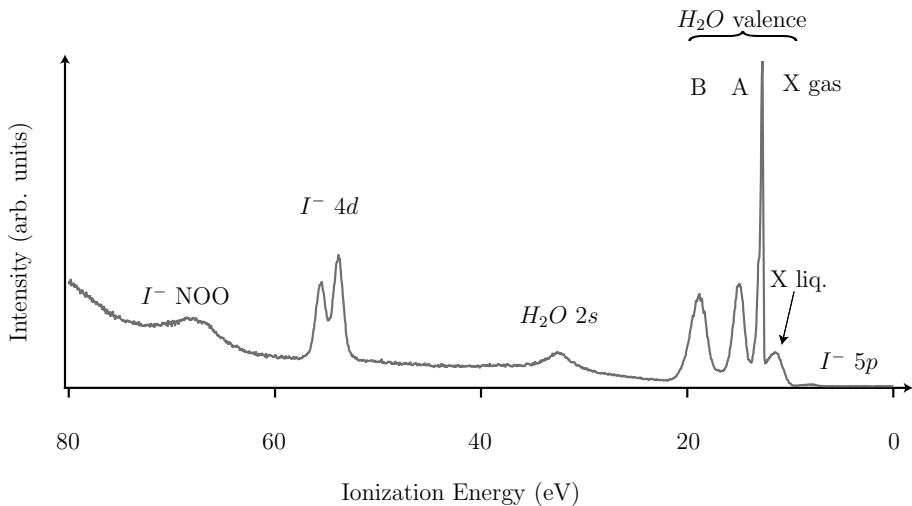

Figure 6.1: Illustration of TBAI structure.

Figure 6.2: The valence spectrum of aqueous TBAI.

Tamaki has studied the surface activity of TBAI at the air/aqueous solution interface [54]. The results showed that the TBA$^+$ ions show a tendency to be rejected from the aqueous phase and transferred to the interface, as a result of the strong water-water cohesive force. Holmberg and co-workers have per-

formed depth profiling of TBAI in formamide solution, where they attributed salt segregation in the surface mono layer to size of TBA$^+$ ion [55]. In this work we have investigated the surface activity of TBAI in water by using photoelectron spectroscopy together with calculations.

The UPS spectrum of aqueous TBAI (concentration 0.04 m) is shown in figure 6.2. The spectrum shows several I$^-$ lines i.e. I$^-$ 5p, I$^-$ 4d, and I$^-$NOO which represents I$^-$ 4d Auger. The C 1s photoelectron spectrum is shown in figure 6.3 and discussed further in more detail below. Moreover, the valence and core ionization energies are listed in table 6.1.

State	Ionization energy (eV)
I$^-$ $5p_{3/2}$	7.6
I$^-$ $5p_{1/2}$	8.4
I$^-$ $4d_{5/2}$	53.7
I$^-$ $4d_{3/2}$	55.4
I$^-$ $4d_{3/2}$	55.4
TBA^+ C 1s	
peak 1	291.9
peak 2	290.7
TBA^+ N 1s	407.4

Table 6.1: *The valence and core ionization energies of aqueous TBAI. The values given for TBA$^+$ C 1s corresponds to peak 1 and 2 respectively.*
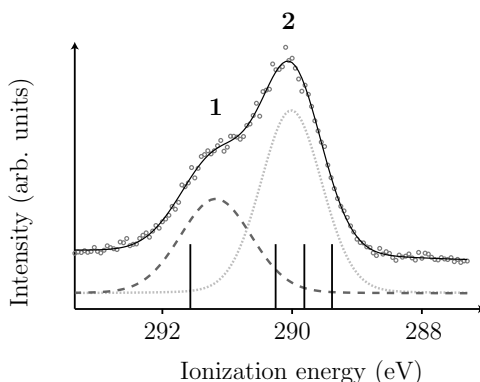

Figure 6.3: The C 1s photoelectron spectrum of aqueous TBAI obtained with 330 eV photon energy.

The C 1s XPS exhibits a peak around 290 eV and a shoulder at higher ionization energy. From the molecular structure of TBAI, we would expect the carbon bonded *(peak 1)* to nitrogen to have higher ionization energy than the

other carbons *(peak 2)*. This is confirmed by a calculation of the total energy difference between the core ionized and the ground state level using Gaussian 03 with B3LYP method and a polarizable dielectric continuum (PCM). The resulting BEs are represented by the vertical relative ionization energies in figure 6.3. However, the experimentally observed relative intensity of *(peak 2)* vs *(peak 1)* does not correspond to the stoichiometric ratio of 3:1.

We assumed that this situation may be caused by inelastic scattering effects. To investigate this, we have recorded spectra using higher photon energies until the relative intensity approaches the stoichiometric value of 3. We recorded ratios of 1.66, 2.06, and 2.22 for 40, 65, and 150 eV KE, respectively. The intensity of the alkane-like carbons is in all cases lower than what we would expect.

We concluded that the molecule is oriented at the surface with the butyl arms sticking into the liquid, even though the butyl arms are hydrophobic. We also found that by increasing TBAI concentration, the peak ratio is decreasing (concentration 0.02 and 0.04 m, peak ratios 2.38 and 2.06, respectively), suggesting an increased tendency of the arms to stick into the liquid with increasing concentration. The molecular dynamics simulations from Ref. [56] supported our experimental results that the orientations of the butyl chains parallel to the surface and never point into the vacuum.

We may have to revise these conclusions, however, since these early data for practical reasons were recorded at 90 degrees instead of at the magic angle of 54.7 degrees between the polarization vector direction and the detector. For free molecules it is well known that for angles others than the magic angle, non-stoichometric ratios may be observed due to differences in angular distribution. Recently we have studied the angular distribution effect for aqueous samples, and we have indeed observed angular-dependent intensity variations between 54.7 and 90 degree. We tentatively attribute this to the combined effects of the intrinsic molecular angular distribution and the extrinsic random elastic scattering of the electron on its way through the sample. In light of this, it would be of interest to record solvated TBA$^+$ from Paper I with "magic angle" and compare with the previous result.

6.2 Aqueous molecules/ions probed by AES: Papers II, III, and V

The majority of the works in this Thesis used Auger electron spectroscopy to investigate molecule and ions in aqueous solutions. To comprehend the characteristics of the Auger process for solvated molecule and ions, this section will discuss fundamental concepts and phenomena regarding Auger spectra of condensed matter.

6.2.1 Fundamental principles of AES of solvated ions

We will start the discussion with weakly van der Waals bonded condensed matter, e.g. argon clusters [57]. The energy of a core-valence-valence (CVV) Auger electron emitted in a certain transition is the energy difference between the core-ionized state and the doubly charged final states with two holes in the valence band. The energy of the core-ionized state differs from the neutral ground state by the XPS BE. In argon, the difference in energy between the ground states of free and condensed atoms (ΔE_{GS0}) is small. In the condensed phase, the energy of the singly core-ionized state will be lowered by polarization screening relative to the case for free atoms by an amount ΔBE^{XPS} (= ΔE_{Q_1}).
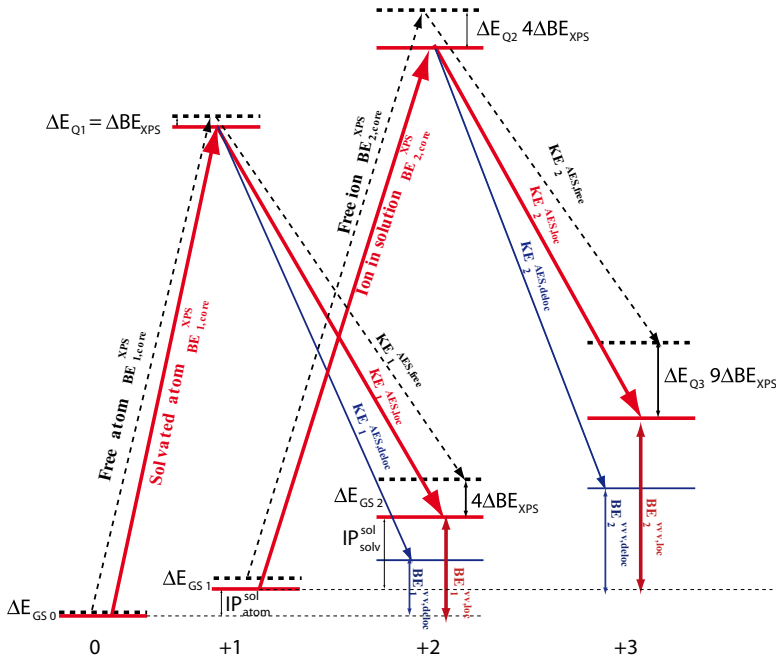

Figure 6.4: Schematic figure of the Auger process. The Auger electron energy (KE^{AES}) is the difference between the XPS binding energy (BE_{core}^{XPS}) and the energy of the two-hole final states (BE^{vv}). The subscripts loc and deloc refer to localized and delocalized final states, respectively.

The magnitude of the polarization screening is proportional to the charge squared, so doubly charged final states with the two holes localized on the same monomer, results in a four times larger shift ($\Delta E_{Q_2} = 2^2 \Delta BE^{XPS}$). Considering the initial and final state, the difference in the resulting Auger electron KE between those states is thus three times the core level BE shift [58]:

$$KE_1^{AES,loc} = \Delta E_{Q_2} - \Delta E_{Q_1} = 3\Delta BE^{XPS} \tag{6.1}$$

The energy of the Auger final state, relative to the neutral ground state, is referred to as the two-hole BE.

$$BE_1^{vv,loc} = BE_{1,core}^{XPS} - KE_1^{AES,loc} \qquad (6.2)$$

For stronger bonds (compared to van der Waals-bonded rare-gas systems) like in water clusters [19] or in solutions, as are the case studied here, it is possible for the two active electrons to originate from different monomers. The BE is typically lower for such a delocalized final state, leading to a higher KE of the corresponding Auger electron. The energy relations between the involved states are illustrated in figure 6.4.

In case of delocalized final state holes, the Coulomb repulsion between the two holes state needs to be considered:

$$BE_1^{vv,deloc} = IP_{atom}^{sol} + IP_{solvent}^{sol} + U_{Coulomb} \qquad (6.3)$$

where IP_{atom}^{sol} and $IP_{solvent}^{sol}$ are the valence ionization energies of the solvated atom and the solvent (also solvated). It is possible to investigate the screening influence of the solvation by comparing the ionization potential (IP) and Auger KE of an ion in the free phase and in solution. As mentioned the singly charged ion will, relative to the free phase in solution, be screened by the polarization of the surrounding water molecules, lowering the energy of the ionic ground state by the amount ΔE_{GS1}, which is similar to ΔE_{Q1} (see figure 6.4). The energy of the doubly charged core-ionized state and the triply charged Auger final state in solution will be lowered by ΔE_{Q_2} and ΔE_{Q_3} respectively. Assuming that polarization screening, which scales by the square of the charge, is the dominating effect, we expect $\Delta E_{Q_2} = 2^2 \Delta BE_{XPS} = 4\Delta BE_{XPS}$ and $\Delta E_{Q_3} = 3^2 \Delta BE_{XPS} = 9\Delta BE_{XPS}$. Thus, as indicated in figure 6.4, a comparison of the core-level ionization potentials and the Auger final state energies of the free and the solvated ion will give us information about the screening. Similar reasoning has for instance been used for argon clusters in Ref. [57] and for water clusters in Ref. [19], where the situation for a free atom or molecule and an atom or molecule in the cluster was compared.

6.2.2 ICD-like core-hole decay in aqueous NH_3: Paper II

The Auger electron spectra of pure ammonia (NH_3) cluster and NH_3 in aqueous solution were investigated in Paper II. However, the discussion in this Thesis is mainly focusing on the delocalized final states in liquid NH_3.

Several years ago, Auger electron spectroscopy was applied to explore water clusters. The CVV Auger spectrum of water clusters has contributions from two-hole final states that are localized on the ionized molecule. There are also final states that are delocalized over several centra, lying at higher KE [19]. Such features are also found in Auger spectra of NH_3 clusters and aqueous

NH$_3$. The Auger spectrum of NH$_3$ cluster has both contributions which pertain to localized transitions, with both final state valence holes on the NH$_3$ molecule that was core ionized, and delocalized ones with one of the final valence holes on a neighboring NH$_3$ molecule.
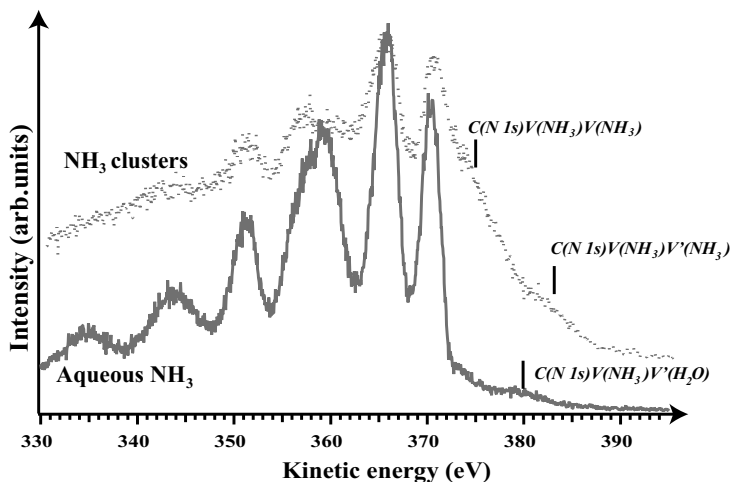

Figure 6.5: Auger electron spectrum of ammonia in aqueous solution. Vertical bars indicate localized C-VV and delocalized C-VV$'$ states.

The Auger spectrum of aqueous NH$_3$ is shown in figure 6.5. The main Auger features located in the 330-375 eV are dominated by the contribution from free NH$_3$ molecules, but a suspicious feature around 380 eV KE , i.e. at higher KE than allowed for free NH$_3$, suggests that NH$_3$ molecules in aqueous solution may be involved. In the light of the discussion for pure NH$_3$ clusters, it is reasonable to assign this feature to delocalized states of the NH$_3\cdots$H$_2$O complex in the liquid. The two outermost valence orbitals of water are; 3a1, which participates in the hydrogen bond (since it is has strong H 1s character), and 1b$_1$, a lone-pair orbital (with O 2p character) [16]. The BE of the 1b$_1$ orbital is higher than the outermost valence orbital of ammonia. Thus, the Auger electrons stemming from a C(N1s)-V(NH$_3$)V$'$(H$_2$O) process should have lower KE than the corresponding C(N1s)-V(NH$_3$)V(NH$_3$) Auger electrons, as presented in figure 6.5.

Therefore, we concluded that transitions to the delocalized final Auger states with one valence hole on the core ionized ammonia molecule and one on an adjacent water molecule (V(NH$_3$)V$'$(H$_2$O)) are found at lower in KE than the comparable states found in pure ammonia clusters, which can be explained by the higher BE of the outermost valence orbital in water relative to ammonia. The decay mechanism leading to such delocalized final states bear resemblances to the Intermoleular Coulumbic Decay (ICD) observed for the decay of inner-valence holes [20, 59, 60], and we will in the following denote them ICD-like.

6.2.3 ICD-like core-hole decay in aqueous K^+: Paper III

As for water clusters [19], ammonia clusters, and ammonia in aqueous solution (Paper II), a suspicious features at higher KE than the main Auger features can be observed in solvated potassium ion in aqueous potassium chloride as well.
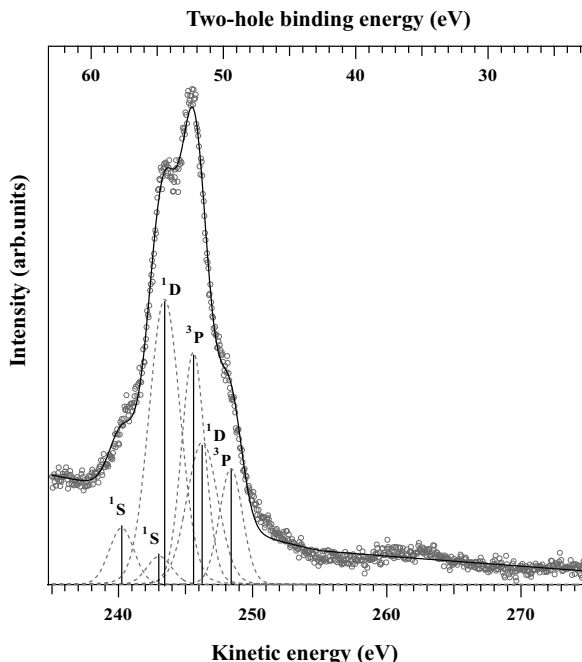

Figure 6.6: The $L_{2,3}M_{2,3}M_{2,3}$ Auger spectrum of K^+ in aqueous KCl, corresponding to the transitions from the $K^{+2} 2p^{-1}$ to the $K^{+3} 3p^{-2}$ localized final state. The dashed lines shows the individual fitted peaks. The solid line gives the resulting fit envelope. The solid vertical bars represent the center of gravity of the multiplet components. The feature at higher kinetic energy corresponds to the transitions from the $K^{+2} 2p^{-1}$ to the $K^{+2} +$ (water valence)$^{-1}$ delocalized final state.

The K 2p and Cl 2p Auger spectra of aqueous KCl are shown in figure 6.6 and 6.7, respectively. The spectra are plotted both on a KE scale (lower axis) and a two-hole BE scale (upper axis), calculated as the difference in energy between the $2p_{3/2}$ core-hole BE and the Auger KE. For free K^+ and Cl^- ions, the lowest lying final state configuration in the Auger process will have two holes in the 3p shell, giving rise to ^1S, ^1D, and ^3P states. Assuming the same states for an aqueous ion, we obtain a good fit to the experimental data. By comparing to corresponding data from molecular and solid KCl [61, 62], we find that the main feature of the K^+ AES spectrum in the aqueous phase more strongly resembles that of the ionic solid than the molecular form.

When comparing the Cl^- AES for the aqueous KCl solution in figure 6.7 with the gas-phase [63] and the ionic solid phase spectra [61], we find that the

spectrum of the aqueous Cl⁻ is less structured. This can partly be attributed to the greater variety in chemical surroundings in the relatively disordered liquid, compared to the gas phase and solid phase.
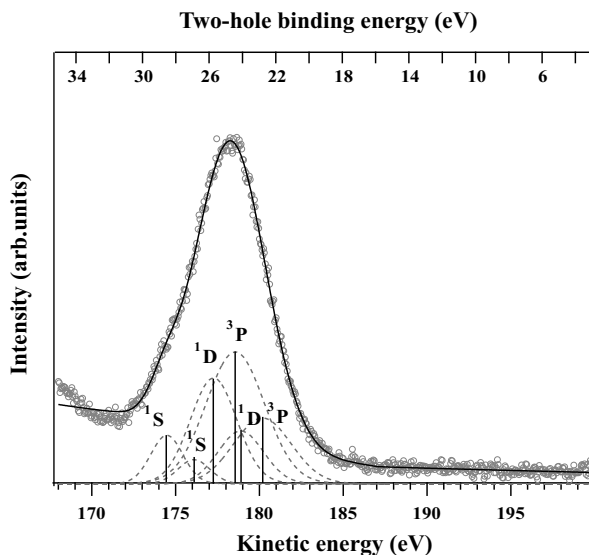

Two-hole binding energy (eV)

Figure 6.7: The $L_{2,3}M_{2,3}M_{2,3}$ Auger spectrum of Cl⁻ in aqueous KCl. The dashed lines shows the individual fitted peaks. The solid line gives the resulting fit envelope. The solid vertical thin lines represent the center of gravity of the multiplet components.

Furthermore a conspicuous additional feature is located at 15-20 eV higher than the main feature is observed. The higher KE means a lower final state energy, and we suspect that this feature is caused by K $3p^{-1}$ H₂O valence $^{-1}$ delocalized final states, as these typically have lower final state energy due to smaller Coulomb repulsion between the final state vacancies. In gas phase KCl, a similar feature was found at 20-25 eV above the main peak, and was assigned to K $3p^{-1}$ Cl $3p^{-1}$ delocalized final states.

To interpret this, calculations of the Auger spectra of the KCl molecule and selected KCl(H₂O)$_n$ (n=1-6) clusters have been performed. For the K⁺ Auger spectrum, the calculations show that the above assignment of the main peak is essentially correct. Furthermore, the calculations reproduce the delocalized final state reported for gas phase KCl. It can also be seen, that when water is added to the system, the delocalized state involving K and Cl start decreasing, and new features, closer to the main line, appear. These features correspond to final states with vacancies on K and water, respectively. These features fit well with the experimentally observed delocalized features. From this we conclude that the delocalized final states are indeed caused by states delocalized over K and the surrounding water molecules produced by ICD-like core-hole decay processes.

Turning back to the Cl 2p AES in figure 6.7, we find that if we estimate the two-hole BEs for states with vacancies at Cl$^-$ and water respectively, analogous to the K$^+$ AES, the delocalized finals states are spectrally overlapping with the main peak. The reason for this overlap is that the final state will be singly charged, meaning that there is no coulomb repulsion even for the localized feature. The calculations also show that a redistribution of intensity between the energetically overlapping localized and delocalized final states of the Auger decay occurs, and this explains why the Cl$^-$ AES delocalized final states can not be observed.

6.2.4 ICD-like core-hole decay in aqueous Ca^{2+}: Paper V

We will now proceed to investigate the influence of ionic charge upon the ICD-like decay, starting the discussion with aqueous Ca^{2+}. The main Ca 2p Auger feature, located in the KE range 275-300 eV has been fitted analogously to K 2p Auger with two series of peaks corresponding to these final states, one for each of the 2p$_{1/2}$ and 2p$_{3/2}$ components which have BE 356.5 and 352.8 eV respectively. The energies obtained from the Auger spectrum fitting of the energy states ^{3}P, ^{1}D, and ^{1}S are 281.9, 285.2, and 287.9 eV respectively, as shown in figure 6.8.

A weak but distinct additional feature is located between KE 300-320 eV, is present in the Ca^{2+} AES shown in figure 6.8 and magnified in the inset. The KE of this feature is not dependent on the photon energy, which establishes that it is due to an Auger- or ICD-like process. The fact that it has higher KE than the main L$_{2,3}$M$_{2,3}$M$_{2,3}$ feature suggests that it is due to an ICD-like decay, involving a vacancy at a neighboring site. In aqueous CaCl$_2$, it is considered that there are no contact ion pairs, even at much higher concentrations than studied here, though solvent-shared ion pairs may exist [64, 65]. For aqueous KCl in Paper III, where a similar situation occurs, the chloride anion orbitals were found to most likely not be involved in a similar observed spectral feature, which would suggest that the feature in the present spectrum is due to final states involving holes on both calcium and water.

The energy of such delocalized two-hole final states can be estimated using the known one-hole BEs for the Ca^{2+} 3p and water (1b$_1$)$^{-1}$ (X), (3a$_1$)$^{-1}$ (A), and (1b$_2$)$^{-1}$ (B) states, see the expanded spectrum in the inset of figure 6.8. One extreme is to treat the two holes as independent, i.e. assuming that they are completely screened and/or infinitely far apart. In this case the two-hole BE is the sum of the one hole BEs. These energies form the low-BE end of each two-hole final states interval. The high-BE end is instead obtained by assuming the energy of two final state holes to be increased by their mutual Coulomb repulsion. A mean Ca-O distance of 2.46 Å [66] gives a Coulomb energy of 17.55 eV. Combining the upper and lower BE limits, we obtain two-hole final states energy intervals for Ca (3p)$^{-1}$ H$_2$O(1b$_1$)$^{-1}$, Ca (3p)$^{-1}$ H$_2$O(3a$_1$)$^{-1}$, and Ca (3p)$^{-1}$ H$_2$O(1b$_2$)$^{-1}$ (denoted CaX, CaA and CaB from
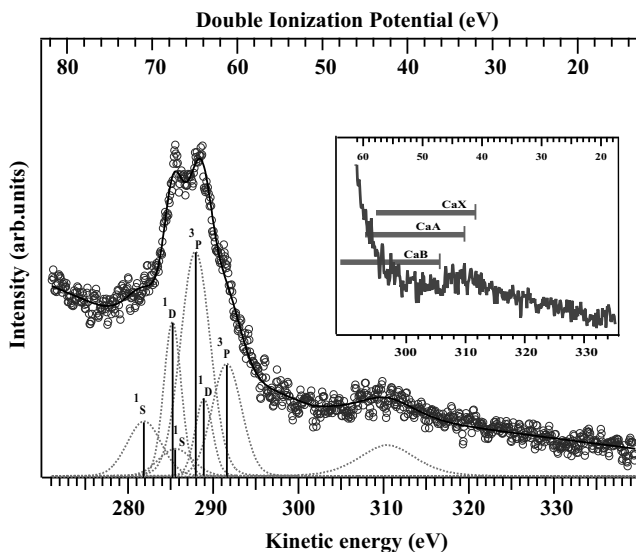
Figure 6.8: The Ca^{2+} Auger spectrum of aqueous $CaCl_2$. The $L_{2,3}M_{2,3}M_{2,3}$ features corresponding to transitions from the Ca^{3+} $2p^{-1}$ to Ca^{4+} $3p^{-2}$ localized final states. The dashed lines show the individual fitted peaks. The solid line gives the resulting fit envelope. The solid vertical bars represent the center of gravity of the multiplet components. The feature at higher kinetic energy corresponds to transition from the Ca^{3+} $2p^{-1}$ to Ca^{4+} $3p^{-1}$ + water valence delocalized final states. This part is expanded in the inset window. The horizontal solid lines show estimated energy ranges for the two-hole states CaX, CaA, and CaB.

now on) of 41.16-58.71, 43.50-61.05, and 47.34-64.89 eV, respectively, as indicated by horizontal bars in the in the inset of figure 6.8. As seen, these energy intervals correspond well with the observed feature.

We therefore interpret this feature as due to the ICD-like decay from the $2p^{-1}$ core-hole state of Ca^{2+} to delocalized final states with one Ca 3p vacancy and one vacancy on a neighboring water molecule.

6.3 The time-scale of ICD-like core-hole decay of aqueous ions: Papers IV and V

The core-hole clock is an effective method to investigate dynamics occurring on the time-scale of the core-hole lifetime [67, 68]. This technique is based on using the relatively well known lifetime of a core-hole as an internal reference to time another dynamic process observed as a separate channel in the core-hole decay spectrum. The relaxation of a core-hole state can for instance be probed by investigating the Auger and ICD decays. For very fast charge

transfer processes, the CK decay, in which the initial and final states are in the same electronic shell, can be used as the internal reference.

This Thesis has been combining XPS and AES together with computational calculations to investigate the time-scale of ICD-like core-hole decay of aqueous Na^+, K^+, Mg^{2+}, Ca^{2+}, and Al^{3+}, as presented in Papers IV and V.

6.3.1 The time-scale of ICD-like core-hole decay of aqueous K^+ and Ca^{2+}

The relative intensity of the different core-hole decay channels, the ICD-like channel leading to delocalized states and the Auger-like channel leading to localized states, are proportional to the relative decay rates, and thus inversely proportional to the respective decay time constants. We can then use the core-hole clock method to set a time-scale by using the relatively well known time-scale of the normal Auger [68, 69].
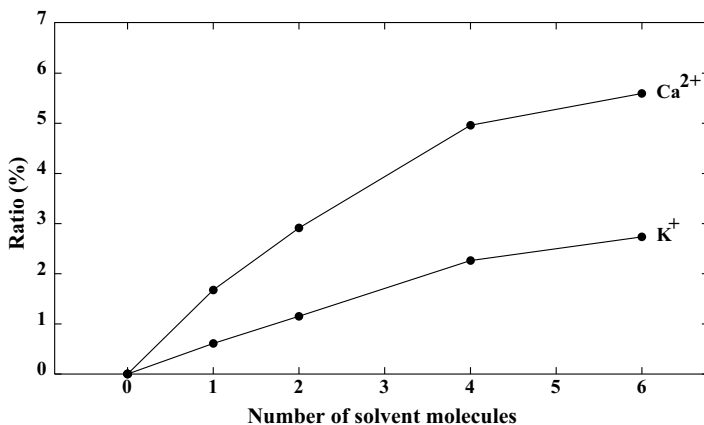

Figure 6.9: The graph shows the relation between the number of solvent molecules and the intensity ratio of the delocalized/localized final states in K^+ and Ca^{2+} 2p core hole decays.

To explore this for both mono and divalent cations, we fitted the K^+ core-hole decay spectrum from Paper III analogously to the Ca^{2+} case in Paper V, and calculated the intensity ratios between the delocalized and localized final states of both cations. The ratios between two channels of aqueous K^+ and Ca^{2+} were 3±1% and 13±3%, respectively. Note that the errors were estimated from the fitting. The core hole life-time widths of K^+ and Ca^{2+} have been taken from data for the free molecules KCl and CaF_2, for which they are 0.18 and 0.21 eV, respectively. Converted to time-scale this is approximately 3.7 and 3.1 fs, respectively [62, 70–73]. Therefore, the K^+ and Ca^{2+} in aqueous solutions have $2p^{-1}$ ICD decay time-scale of roughly 120±40 and 24±6 fs, respectively.

We have computationally investigated the relative importance of the ICD channel ratio for K^+ and Ca^{2+} as a function of the number of solvating water molecules, see figure 6.9. A first observation, is that by increasing number of solvating water molecules, the relative efficiency of the ICD process also increases. A second observation is that the divalent Ca^{2+} cation has a stronger effect than the monovalent K^+ cation, in the sense of yielding higher ICD fractions and thus shorter ICD time constant, in agreement with experiment.

The ICD -like core-hole decay was experimentally found to be five times faster for Ca^{2+} than for K^+. A possible explanation would be that ICD gets increasingly more efficient with increasing number of water neighbors. The first solvation shell for both calcium [65, 66, 74–77] and potassium [74, 78, 79], however, is reported to consist of 6-8 water molecules.

Another possible contributing factor is that a smaller ion-water distance implies a larger overlap between the ion and water orbitals, facilitating the ICD process. Moreover, the positive ionic charge induces a polarization of the water molecules, which increases the electron density on the oxygen atom facing the cation. This increase of electron density in the vicinity of the ion, which occurs already in the ground state, would also facilitate the ICD process. Additionally, while the geometric structure is essentially unchanged relative to the ground state, the electronic structure is affected by the induced polarization of the surrounding water molecules by the intermediate state core-ionized species Ca $(2p^{-1})^{3+}$ and K $(2p^{-1})^{2+}$. The higher charge in combination with the shorter ion-water distance in the calcium case results in a stronger polarization of the water electron density towards the ion, which we consider to qualitatively explain the five-fold increase of the ICD rate from the potassium to the calcium case.

6.3.2 The influence of ICD-like core-hole decay on the core-hole life times of aqueous Na^+, Mg^{2+}, and Al^{3+}

In Paper IV we compared the two outermost core shells of aqueous Na^+, Mg^{2+}, and Al^{3+}, as presented in figure 6.10. Photoelectron spectra 2p and 2s levels of the Na (a), Mg (b), and Al (c) from aqueous solutions recorded in direct sequence under the same conditions, are shown in the right and left part respectively. The Na 2p feature overlaps with the strong O 2s feature of water, and to facilitate the comparison, we have subtracted a spectrum of pure water in the presented spectrum.

A direct comparison shows that the 2s lines are significantly broader than the 2p features, even though the latter are split by the spin-orbit interaction in the final state. We have attempted to determine the lifetime of the 2p and 2s vacancies from the spectral widths, taking many fitting aspects into account.

The reason for the larger lifetime width of the 2s compared to the 2p level in the metals is the fast Coster-Kronig decay of the 2s hole, involving a 2p electron filling the 2s vacancy, and a 3s or 3p electron being ejected, on a time
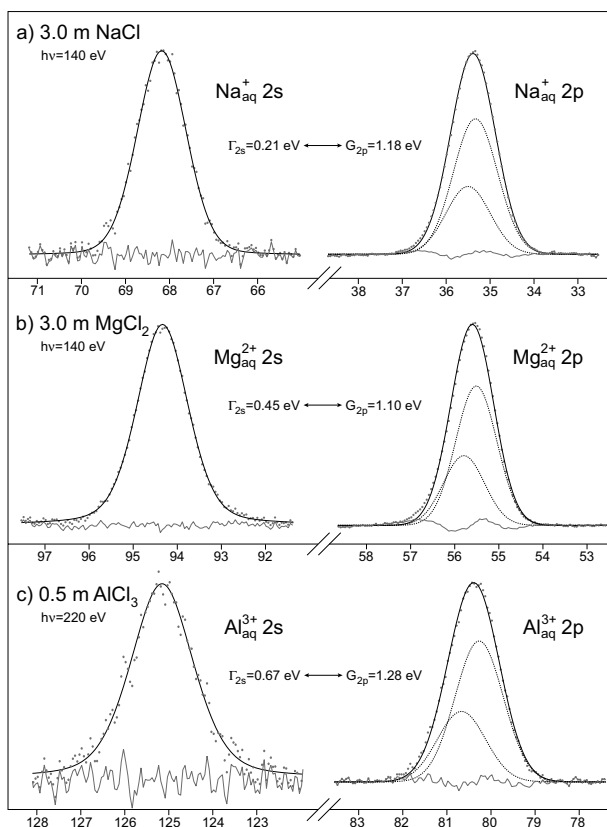
Figure 6.10: Photoelectron spectra of the 2p (right) and 2s (left) levels from aqueous solutions of NaCl, MgCl$_2$, and AlCl$_3$. The solid lines (black) correspond to the total intensities of the fits, and the dot-dashed lines (blue) represent the residues. The data points are represented by filled circles (red). A background has been subtracted in all spectra (see text). In the 2p spectra, the dashed lines (black) represent the Voigt profiles of the 2p spin-orbit components. Note that the scale on the vertical axis differs between the spectra.

scale in the femtosecond range. In free ions, this decay would be impossible, as there are no 3s or 3p electrons to carry away the excess energy. A super-Coster-Kronig decay, involving two 2p electrons, one filling the 2s core hole and one being ejected, is impossible for energetic reasons in the metals as well as for the free or solvated ions. The most obvious explanation of the Lorentzian width of the 2s lines for the solvated ions is that an intermolecular Coster-Kronig process takes place, where instead of the 3s or 3p electron, an electron from the surrounding water molecules or an associated anion is emitted after the 2s vacancy has been filled by an electron from the 2p shell.

The observed widths correspond to lifetimes of the $(2s)^{-1}$ inner valence state of 3.1, 1.5, and 0.98 fs for Na$^+$, Mg^{2+}, and Al^{3+} respectively. The decrease of the lifetime from Na$^+$ to Al^{3+} correlates well with the increased

ion-water interaction. This interaction is dominated by the first solvation shell, which contain approximately the same amount of water molecules (5.4 for Na^+, 6 for Mg^{2+} and Al^{3+}), but the ion-water distance decreases with increasing ionic charge (2.4 for Na^+, 2.1 for Mg^{2+}, and 1.9 for Al^{3+}) [74]. Since Al^{3+} is a smallest ion and has a shortest distance to water, resulting to strongest ion-water interaction, and shortest lifetimes if compared to Na^+ and Mg^{2+}.

6.3.3 Charge-dependence of the time-scale for ICD-like core-hole decay of aqueous ions

As discussed above, the ionic charge has a strong influence on the ICD time-scale. It is therefore reasonable to compare ions of equal charge, i.e. Na^+ to K^+ and Ca^{2+} to Mg^{2+}. The ratio between the ICD time constants is 40 for K^+/Na^+ and 16 for Mg^{2+}/Ca^{2+}. These large ratios are difficult to explain with only the small external differences in solvation number and geometry [74]. We instead attribute the faster ICD process observed for the $2s^{-1}$ core-hole states of Na^+, Mg^{2+}, and Al^{3+} relative to the $2p^{-1}$ core-hole states of K^+ and Ca^{2+} to internal differences in the decay mechanisms of the ions.

Both the $2p^{-1}$ decay of K^+ and Ca^{2+} and the $2s^{-1}$ decay of Na^+, Mg^{2+}, and Al^{3+} involve one electron from the outer of the core-ionized ion and one electron from a water molecule. The difference lies in the relation between the ion orbitals with the initial state core-hole and the final state hole. In the case of the $2p^{-1}$ decay of K^+ and Ca^{2+} discussed here, the final state hole is in the 3p outer orbital, which has a higher main quantum number than the initial 2p core hole. In contrast, the $2s^{-1}$ decay of Na^+, Mg^{2+}, and Al^{3+} results in a final state with a hole in the 2p orbital. The initial and final holes on the ion are thus in orbitals with the same main quantum number, or shell, allowing a much higher orbital overlap and thus a higher decay rate. The difference between the slower $2p^{-1}$ decays of K^+ and Ca^{2+} and the faster $2s^{-1}$ decays of Na^+, Mg^{2+}, and Al^{3+} is thus reminiscent of the difference between the slower Auger and the faster CK processes.

The rate difference between related Auger and CK processes is typically one order of magnitude. For shallow core levels, the time constants of Auger decay is in the order of a few fs, and some tenths of a fs for CK decay. We can thus distinguish between the "Auger-like" and "CK-like" ICD of aqueous ions. The observed time constants of the two processes is in the order of a few fs for the "CK-like" ICD and a few tens of fs for the "Auger-like" ICD. We note that the ratio between the decay rates of "Auger-like" and "CK-like" processes is similar in for the aqueous ions and other systems. However, the absolute rates are approximately one order of magnitude lower for the ICD-like processes involving a neighboring water molecule compared to both ordinary Auger and CK processes not involving orbitals localized on neighboring species.

6.4 Passive and active roles for ions and water in the water O 1s Auger decay: Paper VI

In this work AES has been applied to investigate the branching of the O 1s Auger decays of aqueous LiBr, MgBr$_2$, and ammonium halides (NH$_4$X; X = F, Cl, Br, I). The different possible two-hole final states resulting from O 1s Auger process in the free water molecule, pure liquid water, and aqueous salt solution are illustrated in figure 6.11.
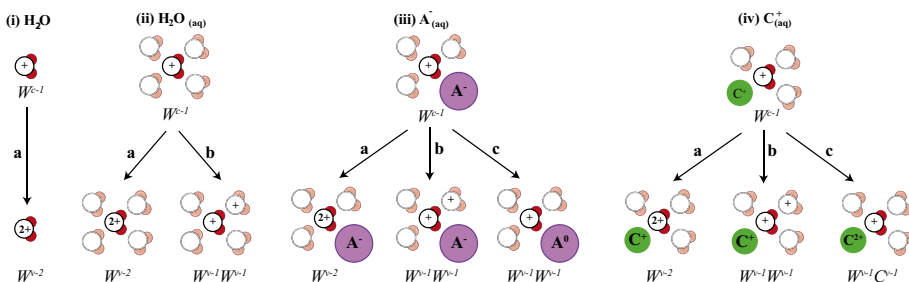

Figure 6.11: Illustration of different possible two-hole final states resulting from H$_2$O oxygen 1s Auger process in the free water molecule (a), in pure liquid water (b), and in aqueous salt solution; (c) and (d) describes the situation when a core-ionized water molecule resides in the first solvation shell of an anion and a cation, respectively.

Core ionization of water molecules results in a highly localized and unstable $(1s)^{-1}$ core-hole cationic state, that quickly relaxes through normal Auger decay in which one valence electron fills the core hole, while another valence electron is emitted. Depending on the chemical environment of the core-ionized molecule, different decay pathways are possible, as schematically shown in figure 6.11. A free core-ionized H$_2$O molecule in the gas phase almost exclusively relaxes through normal Auger-electron decay, producing localized two-hole final states with the two valence vacancies (W^{v-2}) on the same water molecule. The situation is illustrated in branch i**a**.

If the core-ionized molecule is situated in the hydrogen (H) bonding network of liquid water, the localized decays of channel ii**a** will still be possible, but additional decay pathways open up due to the efficient electronic coupling between the H-bonded neighboring water molecules. As illustrated in channel ii**b**, ICD-like Auger decays in H-bonded systems produce delocalized $W^{v-1}W^{v-1}$ final states, i.e. where the two final state valence holes are residing on different water molecules [19]. The increased spatial separation between the two holes reduces the Coulomb repulsion, making these states lower in energy compared to the localized W^{v-2} states. In the O 1s Auger spectrum, transitions to these delocalized states give rise to high-KE features specific to the condensed phase.

For pure water, the region >505 eV consist exclusively of delocalized $W^{v-1}W^{v-1}$ states produced via channel ii**b**, whereas also localized

W^{v-2} states produced via channel ii**a** are situated in the region <505 eV [19]. Conceptually, the introduction of a solute opens new decay possibilities. A primary effect is that the solvated species will passively influence the degree the O 1s decay on a core-ionized water molecule can couple to a neighboring water molecule to form a $W^{v-1}W^{v-1}$ state, simply due to the reduced number of water-water H-bonds in an aqueous electrolyte, i.e. reducing channels iii**b** and iv**b**.

To investigate this passive effect, AES of aqueous LiBr and MgBr$_2$ are compared in figure 6.12. Both samples had the same concentration of Br$^-$, and consequently all changes in the spectra should primarily be due to the different interaction of the two cationic species with water in the first solvation shell. The O 1s Auger spectra of the LiBr and MgBr$_2$ solutions are presented in the upper panel of figure 6.12, whereas in the lower panel, the differences between the O 1s Auger spectra of those solutions minus that of pure water, are compared.
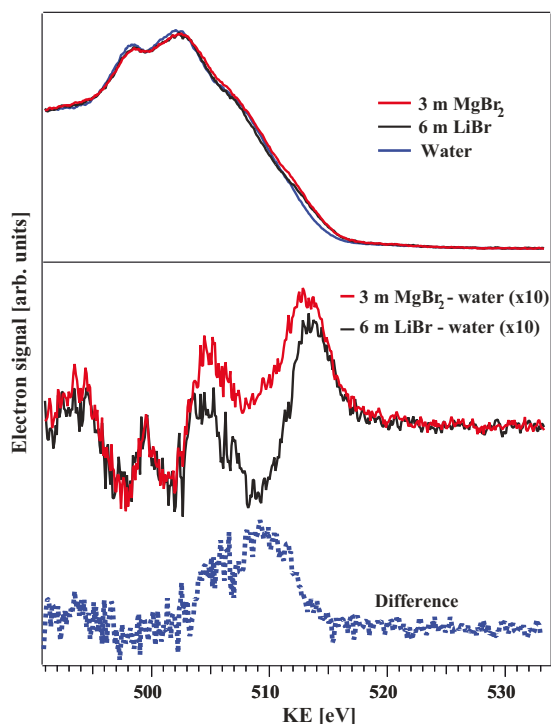
Figure 6.12: Oxygen 1s Auger-electron spectra from water (blue), from 3 m MgBr$_2$ (red) and 6 m LiBr (black) aqueous solutions. The excitation photon energy was 650 eV. The middle part shows the resulting differential spectra, i.e. the solutions minus water. The bottom trace is the difference between the respective two differential solution spectra, i.e. MgBr$_2$ - LiBr.

The main difference between the two cases is a weaker intensity in the 500-520 eV KE region, which also magnified ten times. This interval is connected to the $W^{v-1}W^{v-1}$ states produced by channel ii**b**. We conclude that the metal cations have a passive effect on the water O 1s Auger spectra due to water-water hydrogen bonds being replaced by water-ion bonds. We cannot observe any evidence for a more active role, such as the formation of delocalized de-localized water-cation $W^{v-1}C^{v-1}$ states via decay process iv**b**, of the metal cations in the O 1s Auger decay of water.

To isolate the effects of halide anions on the decay branching ratio, we used identical concentrations of aqueous F$^-$, Cl$^-$, Br$^-$, and I$^-$, in all cases with NH$_4^-$ as counter ion. Figure 6.13 shows the O 1s Auger spectra, as well as the difference spectra between the salt solutions and pure water.
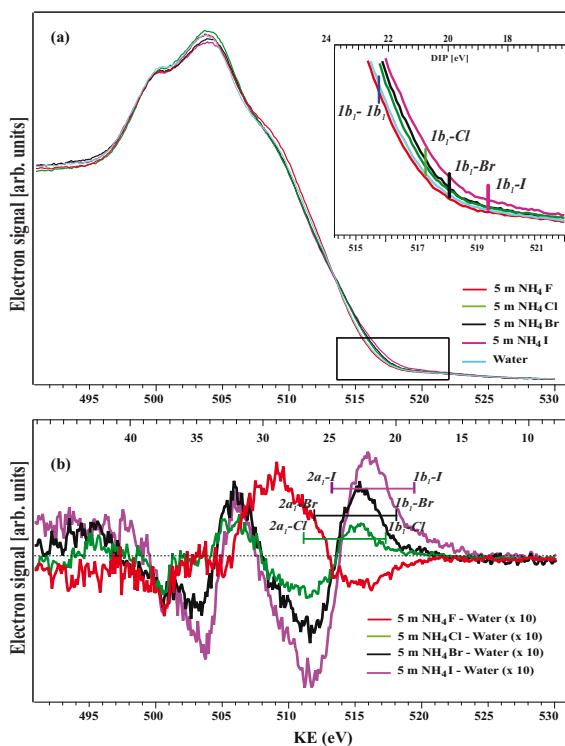
Figure 6.13: Top: Oxygen 1s Auger-electron spectra from pure water (blue) and 5.0 m aqueous ammonium halide solutions NH$_4$I (purple), NH$_4$Br (black), NH$_4$Cl (green), and NH$_4$F (red). All were measured at 650 eV photon energy except NH$_4$I which was recorded at 615 eV. The framed area, covering the 514-522 eV kinetic energy, is shown enlarged in the top right inset, together with the DIP (for explanation of notations *1b$_1$-I*, *1b$_1$-Br*, *1b$_1$-Cl*, and *1b$_1$-1b$_1$*, see text). Bottom: Differential spectra, solution minus pure water from top figure and magnified ten times for better visibility. The DIP energies represented by the horizontal bars shows the lower and upper ener-getic bounds related to the *1b$_1$-X* and *2a$_1$-X* states of the respective solution, where X = I, Br, and Cl.

The passive role of the ions as reducers of water-water coordination would affect the water Auger decay so that the difference spectra would exhibit negative intensity >505 eV, and positive intensity <505 eV. This describes the observed behavior of F^- rather well, although discrepancies, which we will return to later, exist.

The difference spectra for I^-, Br^-, and Cl^- exhibit an almost opposite behavior regarding negative and positive intensity. We start with the positive intensity in the highest KE region 514-525 eV. If the BE of halide X is lower than that of the water HOMO level, the $W^{v-1}A^{v-1}$ delocalized final states will accordingly also be lower in energy than the $W^{v-1}W^{v-1}$ states. This is the case for I^-, Br^-, and Cl^-, and we assign the positive intensities in this region of the difference spectra of figure 6.13(b) to the formation of delocalized $W^{v-1}A^{v-1}$ final states produced via process iii**c**.

We now turn to the 509-514 eV region. For I^-, Br^-, and Cl^-, the difference spectra exhibit negative intensity. This is consistent with the lower water-water coordination in the ionic solutions relative to pure water. While F^- must cause the same reduction in water-water coordination, the difference spectrum of F^- has positive instead of negative intensity in this region. This calls for another mechanism. F^- is the smallest of the halide ions, which in the ground state leads to the smallest ion-water distance, and the strongest destabilization and elongation of the intra-molecular water H-O bond pointing towards the ion. In the intermediate state, the core-ionized water molecule is internally dissociative along one of the intra-molecular O-H bonds. For the proton in the H-O bond oriented towards the negative ion there will be an additional dissociative force due to the Coulomb attraction from the negative ion.

The above arguments can be expressed in a chemically more intuitive form by use of the Z+1 (or equivalent core), approximation. The core-ionized $H_2O(1s^{-1})^+$ species can be approximated as H_2F^+. This allows us to use chemical intuition to understand the dynamics in the core-hole state. The local system immediately after core-ionization can be described as a H_2F^+ ionic radical close to an F^- ion. This is not astable arrangement, but the system will develop towards two neutral molecules by proton transfer, as schematically described by the "reaction formula", in which $O(1s^{-1})$ has been replaced by F:

$$H\text{-}F\text{-}H^+ \cdots F^- \rightarrow H\text{-}F \cdots H^+ \cdots F^- \rightarrow H\text{-}F \cdots H\text{-}F$$
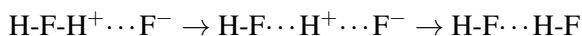
The attractive force between the water proton and the halide ion is inversely proportional to the ion-proton distance, making the effect again strongest for F^-. We propose that the combination of these effects in favorable cases lead to the proton actually leaving the core-ionized H_2O^+, forming core-excited O*H. Estimates of the KE range resulting from Auger decays of aqueous O*H indeed agree well with the 509-514 eV region of positive difference intensity for F^-.

6.5 No ICD-like signature of contact ion pairs: Paper VII

High concentration of aqueous KF, KCl, and KBr solutions were used for investigating contact ion pairs (CIP) in which the constituent ions are in direct contact and not separated by other neutral molecules such as an intervening solvent water molecule in the case of aqueous solutions. If the ions are separated by only a single solvent molecule, the situation is designated as a solvent-shared ion pair (SIP) [80–83].
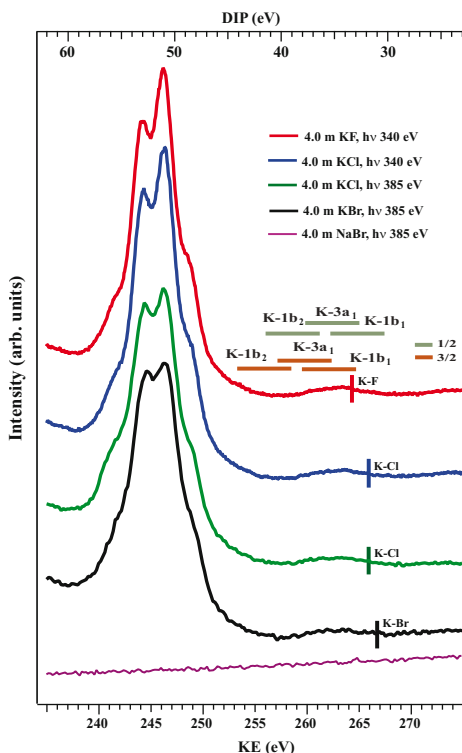

Figure 6.14: (Auger spectra of K^+ after 2p photoionization in aqueous KF, KBr, and KCl . The photon energies used were 340 eV (KF, red spectrum at top, and KCl, blue spectrum, second from top) and 385 eV (KCl, green spectrum, third from top, and KBr, black spectrum, fourth from top). The purple spectrum at the bottom comes from an aqueous 4.0 m NaBr solution, to certify that loss features from Br 3d in the KBr spectrum feature are negligible. Estimated ranges for DIP of delocalized final states involving a vacancy on a water molecules, denoted K-1b$_1$, K-3a$_1$, and K-1b$_2$, are shown as horizontal lines (top scale is for a K 2p$_{3/2}$ intermediate state). The DIP of final states involving the anions are shown as vertical bars.

The main investigation of Paper VII pointed to the distinct features lying between 255-275 eV KE, higher than the main feature in figure 6.14. As shown in Paper III, this feature is due to delocalized Auger final states with

one vacancy in the 3p shell of the core-ionized potassium ion and one valence hole on a neighboring site; $3p^{-1}V^{-1}$, where V stands for a water or anion valence level. Such states have lower energy than $3p^{-2}$ states mainly due to the reduced Coulomb repulsion. The calculation of the Auger spectra were performed for $KCl(H_2O)_{1-6}$ model clusters. For clusters containing a small number of water molecules, such as $KCl(H_2O)_{1-3}$, contributions from states with a Cl^- valence vacancy can clearly be seen in the spectrum, at higher KE than the corresponding water vacancy final states. The intensity of the delocalized states involving a Cl^- vacancy decreased gradually with hydration, and was negligible for a hexahydrated KCl cluster, where delocalized states with a water vacancy dominated (Paper III). The method is thus sensitive to ions in the immediate surrounding and AES could be a suitable tool to investigate this issue.

In figure 6.14, the horizontal bars show DIP intervals for states involving holes in valence orbitals on a neighboring water molecule: $3p^{-1} (1b_1)^{-1}$, $3p^{-1} (3a_1)^{-1}$, and $3p^{-1} (1b_2)^{-1}$, denoted K-1b_1, K-3a_1, and K-1b_2, respectively. The upper and lower bounds of the range correspond to the estimated DIP with and without Coulomb interaction term between the K^{2+} and the $(H_2O)^+$ ions. Additionally, vertical lines indicate estimated DIPs for contact ion pairs, which we have denoted K-F, K-Cl, and K-Br. Note that there will be no Coulomb interaction in the final states, as the anion will become neutral upon losing an electron.

The core photoelectron binding energy of the K^+ 2p level has been reported earlier, 303.55 and 297.74 eV for the K^+ $2p_{1/2}$ and K^+ $2p_{3/2}$ components, respectively (Paper III). The valence binding energies of the aqueous ion levels K^+ 3p, Br^- 4p, and Cl^- 3p were reported at 22.2, 8.8, and 9.6 eV, respectively [51]. The F^- 2p line strongly overlaps with the water 1b_1 emission peak at 11.16 eV [16], and for this reason an accurate value of the outermost valence binding energy of F^- 2p has not been reported in the aqueous phase. In this work we have estimated the F^- valence energy approximately as that of the water X-state (11 eV). We used literature values for the distance of K^+ - water in aqueous KF, KCl, and KI [4–7], to estimate the maximum Coulomb repulsion. The adjacent K^+-water distances have been reported between 2.8-2.9 Å, resulting in a Coulomb repulsive term of 10.3-9.9 eV. The average minimum DIP (maximum in parentheses) for the states K-1b_1, K-3a_1, and K-1b_2 are 33.4 (43.5), 35.7 (45.8), and 39.5 (49.6) eV, respectively. As can be seen, it is thus clear that these features are at least partly due to the Auger decays from the K^{+2} $2p^{-1}$ state to a K^{+3} $3p^{-1}$ and a water valence vacancy state. However, there is still the question whether there are only such states populated, or if CIP states contribute?

In the calculation of the energies of final states with a vacancy on an anion, there is no Coulomb term to consider in the final state, since the anion becomes neutral upon losing an electron. However, there could possibly be a Coulombic contribution in the core-ionize intermediate state. However, this should appear
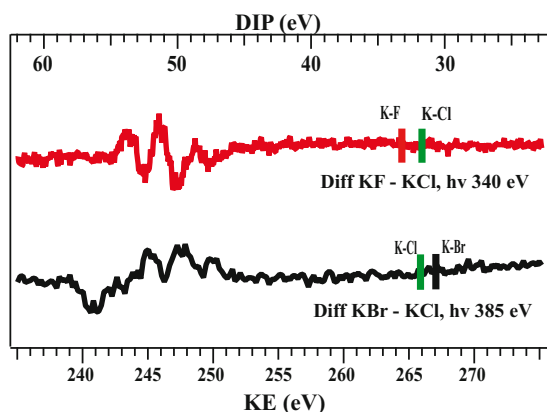
Figure 6.15: (Color online) Difference spectra of aqueous KF minus KCl (top) and aqueous KBr minus KCl (bottom), recorded at the same photon energies, represented by the red and black solid lines respectively. The possible CIP energies are indicated by the vertical bars.

in the photoelectron spectrum as a feature chemically shifted from the line for an ion which is only coordinated to neutral water molecules. We have therefore estimated the DIPs for the possible CIP as the sum of the single hole energies: 33.4, 31.8, and 31.0 eV for K-F, K-Cl, and K-Br, respectively.

In the case of the Cl^- and Br^- counter ions, these energies are clearly lower than the lowest energies for states with water vacancies. By subtracting the spectra from each other, possible minute differences will appear clearer, and we have done so to investigate the possible presence of CIP final states in the K 2p Auger spectra in the structures at high kinetic energy 255-270 eV or DIP 28-43 eV. The difference spectra of aqueous KF minus KCl (red solid line) and aqueous KBr minus KCl (black solid line) in figure 6.15. The spectra show no structure in the region where such final states would appear, which is evidence that CIPs are not common for these potassium salts at the studied concentration. This situation is unlike from Collins *et al.* [84–86] who suggested that the probability to form the CIPs K^+-Br^- and K^+-Cl^- is higher than K^+-F^- because of the K^+, Br^-, and Cl^- were designated as chaotropes, and when the crystalline chaotrope-chaotrope alkali halides (KBr and KCl) dissolve in water, relatively strong water-water interactions will keep the chaotrope ion pairs together. When the constituent ions do dissociate, relatively strong water-water interactions will be broken. In contrast, the F^- ion was designated as a kosmotrope, when a chaotrope-kosmotrope compound (KF) dissolved, the kosmotropic ion of this salt interacts more strongly with water in solution than it did with the chaotrope in the crystal. Consequently, both the solvated K^+ and F^- ions will be preferentially attached to water neighbors.

7. Summary and outlook

All experimental results presented in this Thesis were obtained using photo-electron and Auger spectroscopy based on synchrotron radiation and a liquid micro-jet setup. The results presented in this Thesis fall into two categories: a main one concerning ICD-like process in aqueous systems, and a second smaller one containing the surface study of TBAI.

The first category concerns the final states of the Auger decay process in which the molecule/ions and their neighbors in aqueous solutions were involved. The $(2p)^{-1}$ decay of solvated K^+ and Ca^{2+} ions in aqueous KCl and $CaCl_2$, as well as NH_3 molecule in aqueous ammonia have been studied (Papers II, III, and V). The main Auger features correspond to two-hole final states localized on the molecule/ions, however in addition delocalized final states are also observed at higher kinetic energy. We concluded that in case of delocalization of the two holes resulting from the Auger decay, one is located on the ammonia molecule/solvated cations and the other on a neighboring water molecule, assigned as due to the ICD process. In the case of chloride Auger spectrum, the localized and delocalized final states overlap in energy, preventing their separate identification.

Related phenomena, the contact ion pair formation in highly concentrated of aqueous KCl, KBr, and KF have been studied. No concrete evidence of contact ion pair in K^+ 2p Auger spectra was detected, even though the CIP; K^+-Br^- and K^+-Cl^- were expected as reported in Paper VII.

Papers IV and V applied XPS and AES to compare the time scale for ICD-like core-hole decay processes for monovalent, divalent, and trivalent aqueous ions. We have compared the time-constants of K^+ and Ca^{2+} from the "Auger-like" ICD to those of 2s core holes of the ions Na^+, Mg^{2+}, and Al^{3+} which decay by "CK-like" ICD process. We found that K^+ and Ca^{2+} are slower than Na^+, Mg^{2+}, and Al^{3+}, due to different internal decay mechanisms of the ions, as well as external differences in the ion-solute distances and interactions.

In addition, a study of different roles of aqueous anions and cations in the interaction with water molecules in connection to O 1s core-hole decay is presented in Paper VI. In the O 1s Auger spectra of water and aqueous ammonium halide solutions (NH_4X; X = F, Cl, Br, I), we have observed the extra features at high kinetic energy, similar to those for the solvated cations (K^+ and Ca^{2+}), which are related to delocalized two-hole final states with vacancies on a water molecule and a neighboring solvated anion. The relative intensity of these

feature indicate that the strength of the interaction between halide ions and water decreases as: $I^- > Br^- > Cl^- > F^-$.

The last category, the physical property of hydrophobia (or hydrophilia) is expected to be characterized by a surface enrichment (or depletion) of a molecule after solvation. By varying the photon energy in photoelectron spectroscopy, it is possible to depth profile a liquid solution and thereby address questions related to surface activity. Therefore, XPS and UPS have applied to investigate the surface activity of aqueous TBAI in Paper I. We have found that the TBA^+ is oriented at the surface with the butyl arms sticking into the liquid, even though the butyl arms are hydrophobic.

The main investigated phenomenon in this Thesis is ICD-like charge delocalization dynamics of aqueous solutions. In a broader perspective, several aqueous solutions and systems are of interest, such as organic matter and heavy metals in the environment. Moreover, acid rain caused by sulphate and bisulphate compound, could also be interesting to study because better microscopic knowledge may be used to guide efforts aimed at improving health and environment. Nanoparticles are important systems valuable to investigate as well, because they play an important role in many systems, e.g. optical [87], magnetic [88], and are widely used for biological applications [89].

Angular distribution effects is also an important phenomenon to study. As mentioned in chapter 6, we recently have found angular distribution effect for aqueous samples. The angular-dependent intensity measured at 54.7 ° differs from that at 90 °. Most of photoelectron spectra in this Thesis were recorded under "magic angle" 54.7 ° in order to avoid angular anisotropy effects, except in Paper I which we used 90 °. Therefore, it would be of interest to record solvated TBA^+ from Paper I with "magic angle" and compare with the previous result.

However, to reach a full understanding concerning the structure and bonding in liquids, photoelectron and Auger spectroscopies could possibly consolidate the theoretical analysis together with other experimental techniques, such as photo-absorption spectroscopy e.g. near edge x-ray absorption fine structure (NEXAFS) and extended x-ray absorption fine structure (EXAFS), which provide information on occupied states as well as unoccupied states [90, 91].

Acknowledgements

This Thesis is the results of *a team work*.

(gossiping is included) and being such a great friend. Alin, N Aom, N Jum, and P Ping for humorous stories and a huge laughing stock. Other Thai students; N Noina, N Coam, P Tor-P Ae, P Aran, P Nok, M, N Grace, N Wow, N Air(s), and N SomO, your friendship is most precious to me. Ar Slil-Ar Tus, Pa Da-P On, P Took-Noi, Ant Pa, Pa Nang, and P Jang, I am very grateful for your sympathy.

A last year here, I have a mirthful moment because of Olsson family and relatives (Marianne, Göran, Ann, Rolf, Erik, Linda, Elias, Anders, Karin, and Olof). Thank you for your thoughtfulness and treating me as one of the family member, as well as showing me the Swedish traditions which I could not learn from the university or any book. This is the best experience in my life, I am forever grateful.

Thanks to Anders for your emotional support and assistance when I was writing the Thesis. You are an extremely nice person, I am very happy to have you.

Lastly, I am heartily thankful to my lovely family: Mum, dad, Jib, and Jub, for your big love, perfect support, and great taking care of me. You are the best. I love you.

WITHOUT ALL OF YOU, I COULDN'T COME THIS FAR.

Bibliography

[1] J.-H. Guo, Y. Luo, A. Augustsson, J.-E. Rubensson, C. Såthe, H. Ågren, H. Sieg-bahn, and J. Nordgren. *Phys. Rev. Lett.*, 89:137402, 2002.

[2] T. K. Ghanty, V. N. Staroverov, P. R. Koren, and Ernest R. Davidson. *J. Am. Chem. Soc.*, 122:1210, 2000.

[3] J. C. Slater. *J. Chem. Phys.*, 41:3199–3204, 1964.

[4] H. Ohtaki and N. Fukushima. *J. Sol. Chem.*, 21:23, 1992.

[5] H. Ohtaki and T. Radnai. *Chem. Rev.*, 93:157–1204, 1993.

[6] H. Ohtaki. *Monatshefte für Chemie*, 132:1237–1268, 2001.

[7] M. Ya. Fishkis and T. E. Soboleva. *Zh. Strukt. Khim.*, 15:186, 1974.

[8] R. Moberg. *Bulk Struture and Surface Activity in Liquid Solutions Studied by Electron Spectroscopy, Ph D Thesis*. Acta Universitatis Upsaliensis, Uppsala, 1990.

[9] S. Holmberg. *Electron Spectroscopy of solvated Ions and Liquid Surface, Ph D Thesis*. Acta Universitatis Upsaliensis, Uppsala, 1987.

[10] K. Siegbahn. *Rev. Mod. Phys.*, 54:709, 1982.

[11] K. Siegbahn, C. Nordling, A. Fahlman, R. Nordberg, K. Hamrin, J. Hedman, G. Johansson, T. Bergmark, S. E. Karlsson, I. Lindgren, and B. Lindberg, editors. *ESCA-atomic, molecular, and solid state structure studied by mean of electron spectroscopy*. Almqvist och Wiksells, Uppsala, 1967.

[12] K. Siegbahn, C. Nordling, G. Johansson, J. Hedman, P. F. Hedén, K. Hamrin, U. Gelius, T. Bergmark, L. O. Werme, R. Manne, and Y. Baer, editors. *ESCA Applied to free molecules*. North-Holland Publ. Co., Amsterdam-London, 1969.

[13] S. Hüfner. *Photoelectron spectroscopy*. Springer Verlag, Berlin, 1995.

[14] D. W. Turner, C. Baker, A. D. Baker, and C. R. Brundle. *Molecular Photoelectron Spectroscopy*. Wiley-Interscence, London, 1970.

[15] L. Asplund. *Electron Spectroscopy of Liquids and Gases, Ph D Thesis*. Acta Universitatis Upsaliensis, Uppsala, 1977.

[16] B. Winter, R. Weber, W. Widdra, M. Dittmar, M. Faubeland, and I. V. Hertel. *J. Phys. Chem. A*, 108:2625, 2004.

[17] M. Faubel and B. Steiner. *Ber. Bunsenges. Phy. Chem.*, 96:1167, 1992.

[18] G. Öhrwall, M. Tchaplyguine, M. Lundwall, R. Feifel, H. Bergersen, T. Rander, A. Lindblad, J. Schulz, S. Peredkov, S. Barth, S. Marburger, U. Hergenhahn, S. Svensson, and O. Björneholm. *Phys. Rev. Lett.*, 93:173401, 2004.

[19] G. Öhrwall, R. F. Fink, M. Tchaplyguine, L. Ojamäe, M. Lundwall, R. R. T. Marinho, A. Naves de Brito, S. L. Sorensen, M. Gisselbrecht, R. Feifel, T. Rander, A. Lindblad, J. Schulz, L. J. Sæthre, N. Mårtensson, S. Svensson, and O. Björneholm. *J. Chem. Phys.*, 123:054310, 2005.

[20] L. S. Cederbaum, J. Zobeley, and F. Tarantelli. *Phys. Rev. Lett.*, 79:4778, 1997.

[21] V. Schmidt. *Electron Spectrometry of Atoms using Synchrotron Radiation*. Cambridge University Press, Cambridge, 1997.

[22] E. F. Aziz. *Local Electronic and Geometric Structure of Ions, Molecules, and Polymers in Liquid Phase, Ph D Thesis*. Freie University, Berlin, 2007.

[23] J. Bozek, T. X. Carroll, J. Hahne, L. J. Sæthre, J. True, and T. D. Thomas. *Phys. Rev. A*, 57:157, 1998.

[24] M. Abu-samha. *Lineshape Models in Inner-shell Photoelectron Spectra of Free Molecules and Clusters, Ph D Thesis*. University of Bergen, Bergen, 2006.

[25] H. Bergersen. *Free Neutral Clusters and Liquids Studied by Electron Spectroscopy and Lineshape Modeling, Ph D Thesis*. Acta Universitatis Upsaliensis, Uppsala, 2008.

[26] P. W. Atkins. *Physical chemistry, sixth ed.* Oxford university press, New York, 1999.

[27] M. Lundwall. *Rare-gas Clusters Studied by Electron Spectroscopy: Structure of Heterogeneous Clusters and Effects of Electron Scattering on Auger Decay, Ph D Thesis*. Acta Universitatis Upsaliensis, Uppsala, 2007.

[28] D. M. Mills. *Third-generation hard X-ray synchrotron radiation source - Source properties, optics and experimental Techniques*. Wiley-Interscence, New York, 2002.

[29] Austraian synchrotron. *http://www.synchrotron.vic.gov.au/*, 2008.

[30] A. Hofmann, editor. *The physics of synchrotron radiation*. Cambridge University Press, Cambridge, 2004.

[31] Swedish Synchrotron Radiation Facility (MAX-lab). *http://www.maxlab.lu.se/*, 2008.

[32] M. Bässler, J. O. Forsell, O. Björneholm, R. Feifel, M. Jurvansuu, S. Aksela, S. Sundin, S. L. Sorensen, R. Nyholm, A. Ausmees, and S. Svensson. *J. Electron Spectrosc. Relat. Phenom.*, 101-103:953, 1999.

[33] M. Bässler, A. Ausmees, M. Jurvansuu, R. Feifel, J. O. Forsell, P. T. Fonseca, A. Kivimäki, S. Sundin, S. L. Sorensen, R. Nyholm, O. Björneholm, S. Aksela, and S. Svensson. *J. Nucl. Instrum. Methods Phs Res. A*, 469:382, 2001.

[34] M. Ekelund. *Development of a liquid Microjet source for Electron Spectroscopy, Master Degree Thesis*. Uppsala University, SWEDEN, 2003.

[35] Wikipedia website; http://en.wikipedia.org/wiki/BESSY. 2010.

[36] BESSY website; http://www.helmholtz berlin.de/. 2010.

[37] R. Follath and F. Senf. *Nucl. Instr. Meth. A*, 390:388, 1997.

[38] M.R. Weiß, R. Follath, F. Senf, and W. Gudat. *J. Electr. Spectrosc. Relat. Phenom.*, 101-103:1003, 1999.

[39] R. Weber. *Photoelectron Spectroscopy of Liquid Water and Aqueous Solutions in Free Microjets Using Synchrotron Radiation, Ph D Thesis*. Freie University, Berlin, 2003.

[40] A. Lindblad. *A Treatise on the Geometric and Electronic Structure of Clusters: Investigated by Synchrotron Radiation Based Electron Spectroscopy , Ph D Thesis*. Acta Universitatis Upsaliensis, Uppsala, 2008.

[41] M. Faubel, B. Steiner, and J.P. Toennies. *J Chem Phys*, 106:9013, 1997.

[42] Lord Rayleigh. *Proc. London Math. Soc.*, 10:4, 1879.

[43] Lord Rayleigh. *Philos. Mag.*, 34:145, 1892.

[44] G. N. Chermenskii. *J. Appl. Mech. Tech. Phys.*, 11:179, 1970.

[45] C. Weber. *Z. Angew. Math. Mech.*, 11:136, 1931.

[46] M. Faubel, B. Steiner, and J. P. Toennis. *J. Electron Spectrosc. Relat. Phenom.*, 95:159, 1998.

[47] H. Siegbahn and K. Siegbahn. *J. Electron Spectrosc Relat Phenom*, 2:319, 1973.

[48] B. Lindberg, L. Asplund, H. Fellner-Felldeg, P. Kelfve, H. Siegbahn, and K. Siegbahn. *J. Chem Phys lett*, 39:8, 1976.

[49] H. Siegbahn, S. Svensson, and M. Lundholm. *J. Electron Spectrosc Relat Phenom*, 24:205, 1981.

[50] R. Weber, B. Winter, P. M. Schmidt, W. Widdra, I. V. Hertel, M. Dittmarand, and M. Faubel. *J. Phys. Chem B*, 108:4729, 2004.

[51] B. Winter, R. Weber, I. V. Hertel, M. Faubel, R. P. Jungwirth, E. C. Brown, and S. E. Bradforth. *J. Am. Chem. Soc.*, 127:7203, 2005.

[52] Microliquids GmbH website; http://microliquids.com. 2010.

[53] N. Ottosson. *Structure, excited-state dynamics and surface composition of simple aqueous systems, Licentiate Thesis*. Uppsala University, SWEDEN, 2009.

[54] K. Tamaki. *Bull. Chem. Soc. Japan*, 40:38, 1967.

[55] S. Holmberg, R. Moberg, Z. C. Yuan, and H. Siegbahn. *J. Electron Spectrosc.*, 47:27, 1988.

[56] B. Winter, R. Weber, P. M. Schmidt, I. V. Hertel, M. Faubel, L. Vrbka, and P. Jungwirth. *J. Phys. Chem B*, 108:14558, 2004.

[57] M. Lundwall, M. Tchaplyguine, G. Öhrwall, A. Lindblad, S. Peredkov, T. Rander, S. Svensson, and O. Björneholm. *Surf. Sci.*, 594:12, 2005.

[58] O. Björneholm, F. Federmann, S. Kakar, and T. Möller. *J. Chem. Phys.*, 111:546, 1996.

[59] S. Marburger, O. Kugeler, U. Hergenhahn, and T. Möller. *Phys. Rev. Lett.*, 90:203401, 2003.

[60] S. Barth, S. Joshi, S. Marburger, V. Ulrich, A. Lindblad, G. Öhrwall, O. Björneholm, and U. Hergenhahn. *J. Chem. Phys.*, 122:241102, 2005.

[61] M. Elango, R. Ruus, A. Kikas, A. Saar, A. Ausmees, and I. Martinson. *J. Phys. Rev. B*, 53:R5978, 1996.

[62] E. Kukk, M. Huttula, H. Aksela, S. Aksela, E. Nõmmiste, and A. Kikas. *J. Phys. B.*, 36:L85–L91, 2002.

[63] M. Kivilompolo, A. Kivimäki, H. Aksela, M. Huttula, S. Aksela, and R. F. Fink. *J. Chem. Phys.*, 113:662, 2000.

[64] J. L. Fulton, S. M. Heald, Y. S. Badyal, and J. M. Simonson. *J. Phys. Chem. A*, 107:4688, 2003.

[65] Y. S. Badyal, A. C. Barnes, G. J. Cuello, and J. M. Simonson. *J. Phys. Chem.*, 108:11819, 2004.

[66] F. Jalilehvand, D. Spångberg, P. Lindqvist-Reis, K. Hermansson, I. Persson, and M. Sandström. *J. Am. Chem. Soc.*, 123 (3):431, 2001.

[67] P. A. Brühwiler, O. Karis, and N. Mårtensson. *Reviews of Modern Physics*, 74:703, 2002.

[68] O. Björneholm, A. Nilsson, A. Sandell, B. Hernnäs B, and N. Mårtensson. *Phys. Rev. Lett.*, 68:1892, 1992.

[69] C.-O. Almbladh and A. L. Morales. *Phys. Rev. B*, 39:3503, 1989.

[70] E. Kukk, S. Aksela, H. Aksela, E. Nõmmiste, A. Kikas, A. Ausmees, and M. Elango. *J. Phy. Rev. B*, 50:9079, 1994.

[71] M. Elango, A. Ausmees, A. Kikas, E. Nõmmiste, R. Ruus, A Saar, J.F. van Acker, J. N. Andersen, R. Nyholm, and I. Martinson. *Phys. Rev. B*, 47:11736, 1993.

[72] A. Kikas, A. Ausmees, M. Elango, E. Nõmmiste, R. Ruus, and A Saar. *J. Electron Spectrosc. Relat. Phenom.*, 68:287, 1994.

[73] M. Patanen, J. Niskanen, M. Huttula, K. Jänkälä, S. Urpelainen, H. Aksela, and S. Aksela. *J. Phys. B: At. Mol. Opt. Phys.*, 41:215103, 2008.

[74] Y. Marcus. *Chem. Rev.*, 109:1346, 2009.

[75] G. Licheri, G. Piccaluga, and G. Pinna. *J. Chem. Phys.*, 64:2437, 1976.

[76] P. R. Smirnov and V. N. Trostin. *Russian Journal of General Chemistry*, 79:1600, 2009.

[77] R. Caminiti, G. Licheri, G. Piccaluga, and G. Pinna. *Chem. Phys. Lett.*, 47:275, 1997.

[78] A. K. Soper and K. Weckström. *Biophys. Chem.*, 124:180, 2006.

[79] P. R. Smirnov and V. N. Trostin. *Russian Journal of General Chemistry*, 77:2101, 2007.

[80] T. E. Hogen-Esch and J. Smid. *J. Am. Chem. Soc.*, 88:307, 1966.

[81] T. E. Hogen-Esch and J. Plodinec. *J. Am. Chem. Soc.*, 100:7633, 1978.

[82] D. H. O′Brien, C. R. Russell, and A. J. Hart. *J. Am. Chem. Soc.*, 101:633, 1979.

[83] A. D. McNaught and A. Wilkinson, editors. *IUPAC Compendium of Chemical Terminology, 2nd Revised Edition*. WileyBlackwell, United Kingdom, 1997.

[84] K. D. Collins, G. W. Neilson, and J. E. Enderby. *Biophys. Chem.*, 128:95, 2007.

[85] K. D. Collins. *Q. Rev. Biophys.*, 72:65, 1997.

[86] K. D. Collins and M. W. Washabaugh. *Q. Rev. Biophys.*, 18:323, 1985.

[87] W. J. Parak, D. Gerion, T. Pellegrino, D. Zanchet D, C. Micheel, C. S. Williams, R. Boudreau, M. A. Le Gros, C. A. Larabell, and A. P. Alivisatos. *Nanotechnology*, 14:R15–R27, 2003.

[88] Q. A. Pankhurst, J. Connolly, S. K. Jones, and J. Dobson. *J. Phys. D: Appl. Phys.*, 36:R167–R181, 2003.

[89] O.V. Salata. *Nanotechnology*, 2:3:1–6, 2004.

[90] E. F. Aziz, M. Freiwald, S. Eisebitt, and W. Eberhardt. *J. Phy. Rev. B*, 73:075120, 2006.

[91] E. F. Aziz, S. Eisebitt, F. de Groot, J. W. Chiou, C. Dong, J. Guo, , and W. Eberhardt. *J. Phys. Chem. B*, 111(17):4440, 2007.

Acta Universitatis Upsaliensis

*Digital Comprehensive Summaries of Uppsala Dissertations
from the Faculty of Science and Technology* 726

Editor: The Dean of the Faculty of Science and Technology

ACTA
UNIVERSITATIS
UPSALIENSIS
UPPSALA
2011